Stress release process along an intraplate fault analogous to the plate boundary: a case study of the 2017 M5.2 Akita-Daisen earthquake, NE Japan

doi: 10.1029/2020JB019527

JGR Solid Earth

RESEARCH ARTICLE
10.1029/2020JB019527

Key Points:
- Relocated hypocenters and focal mechanisms indicate that the mainshock, foreshocks, and aftershocks occur on the same intraplate fault
- The foreshocks, mainshock, aftershocks, and postseismic slip released stress on different fault segments
- Foreshock and aftershock seismicity migrate along the fault plane, suggesting that aseismic slip occurs before and after the mainshock

Supporting Information:
- Supporting Information S1

Correspondence to:
K. Yoshida,
keisuke.yoshida.d7@tohoku.ac.jp

Citation:
Yoshida, K., Taira, T., Matsumoto, Y., Saito, T., Emoto, K., & Matsuzawa, T. (2020). Stress release process along an intraplate fault analogous to the plate boundary: A case study of the 2017 *M*5.2 Akita-Daisen earthquake, NE Japan. *Journal of Geophysical Research: Solid Earth*, *125*, e2020JB019527. https://doi.org/10.1029/2020JB019527

Received 3 FEB 2020
Accepted 19 APR 2020
Accepted article online 23 APR 2020

Stress Release Process Along an Intraplate Fault Analogous to the Plate Boundary: A Case Study of the 2017 *M*5.2 Akita-Daisen Earthquake, NE Japan

Keisuke Yoshida[1], Taka'aki Taira[2], Yoshiaki Matsumoto[1], Tatsuhiko Saito[3], Kentaro Emoto[1], and Toru Matsuzawa[1]

[1]Department of Geophysics, Graduate School of Science, Tohoku University, Sendai, Japan, [2]Berkeley Seismological Laboratory and Department of Earth and Planetary Science, University of California, Berkeley, CA, USA, [3]National Research Institute for Earth Science and Disaster Resilience, Tsukuba, Japan

Abstract Stress accumulation and release inside the plate remains poorly understood compared to that at the plate boundaries. Spatiotemporal variations in foreshock and aftershock activities can provide key constraints on time-dependent stress and deformation processes inside the plate. The 2017 *M*5.2 Akita-Daisen intraplate earthquake in NE Japan was preceded by intense foreshock activity and triggered a strong sequence of aftershocks. We examine the spatiotemporal distributions of foreshocks and aftershocks and determine the coseismic slip distribution of the mainshock. Our results indicate that seismicity both before and after the mainshock was concentrated on a planar structure with N-S strike that dips steeply eastward. We observe a migration of foreshocks toward the mainshock rupture area, suggesting the possibility that foreshocks were triggered by aseismic phenomena preceding the mainshock rupture. The mainshock rupture propagated toward the north, showing less slip beneath foreshock regions. The stress drop of the mainshock was 1.4 MPa, and the radiation efficiency was 0.72. Aftershocks were intensely triggered near the edge of large coseismic slip regions where shear stress increased. The aftershock region expanded along the fault strike, which can be attributed to the postseismic aseismic slip of the mainshock. We find that the foreshocks, mainshock, aftershocks, and postseismic slip released stress at different segments along the fault, which may reflect differences in frictional properties. Obtained results were similar to those observed for interplate earthquakes, which supports the hypothesis that the deformation processes along plate boundaries and intraplate faults are fundamentally the same.

1. Introduction

Earthquakes are natural phenomena that release stress and strain energy accumulated inside the Earth (Knopoff, 1958; Savage, 1969). Interplate earthquakes release the stress accumulated by the slip deficit along the plate interface, while intraplate earthquakes, which occur on multiple three-dimensionally distributed faults, release stress and strain energy accumulated within the plates. Quantification of stress accumulation and release is required for a comprehensive understanding of the deformation processes that take place in the Earth.

The accumulation and release of stress at plate boundaries is relatively well understood compared to that inside the plate. At plate boundaries, increase in stress can be monitored as part of geodetic analysis by estimating slip deficit (Matsu'ura & Sato, 1989; Savage, 1983). Analyses of recent dense geodetic network data revealed that the slip deficit rate exhibits substantial spatial variations along the plate boundary (e.g., Suwa et al., 2006; Ryder & Bürgmann, 2008: Noda et al., 2018), which probably reflects variation in frictional properties (Lay & Kanamori, 1981). The stress accumulated at plate boundaries is released by both interplate earthquakes and aseismic slips, and the rupture areas of large interplate earthquakes correlate well with regions of high slip deficit (Hashimoto et al., 2009). Earthquakes cause slip and release stress at same locations repeatedly (Nadeau & Johnson, 1998; Matsuzawa et al., 2002; Yamanaka & Kikuchi, 2004), indicating that the frictional properties along plate boundaries remain the same over long periods of time.

Furthermore, recent geodetic and seismological studies have revealed that not only earthquakes but also abundant aseismic phenomena occur along plate boundaries (e.g., Ide et al., 2007; Beroza & Ide, 2011).

These include postseismic slip (e.g., Heki et al., 1997; Hsu et al., 2006; Wesson, 1987), preseismic slip (e.g., McGuire & Jordan, 2000; Uchida et al., 2004), and episodic aseismic slip events (e.g., Hirose et al., 1999; Linde et al., 1996). The diversity in slip styles at plate boundaries is attributed to heterogeneity in stress state, and frictional and rheological properties of the boundary material (Ando et al., 2010; Liu & Rice, 2005; Marone et al., 1991; Matsu'ura et al., 1992; Shibazaki & Iio, 2003; Perfettini & Avouac, 2004; Tse & Rice, 1986). Such aseismic phenomena may also play important roles in the accumulation and release of stress inside the plate (e.g., Iio et al., 2002; Meneses-Gutierrez & Sagiya, 2016).

The roles of intraplate faults in the accumulation and release of stress, however, are poorly understood compared to interplate faults. One difficulty in the assessment of the temporal evolution of stress on an intraplate fault comes from the weakness of the geodetic signal produced by any aseismic slip, which may occur along an intraplate fault. This is due to the deformation rate inside the plate, which is substantially lower than at plate boundaries. However, certain time-dependent aspects of seismicity can be used to extract information about aseismic phenomena. For example, the migration patterns of hypocenters have been used for the detection and quantification of aseismic slip propagation (Kato et al., 2012; Lohman & McGuire, 2007; Vidale et al., 2006) and pore pressure diffusion (e.g., Chen et al., 2012; Parotidis et al., 2003; Shelly, Hill, et al., 2013; Shelly, Moran, & et al., 2013; Yukutake et al., 2011).

The distribution of fault structures inside the plate adds further complexity to its stress state. Hypocenters of intraplate earthquakes are often scattered three-dimensionally within the plate; this distribution is sometimes referred to as a seismicity cloud. Each earthquake within a seismicity cloud can have different fault plane orientations. Intraplate seismicity does not always occur in a well-defined plane, but some seismicity clouds within the plate merely represent hypocenter estimation errors. In fact, by performing precise hypocenter relocation, previous studies have succeeded in delineating planar structures from seismicity clouds (e.g., Asanuma et al., 2001; Moriya et al., 2006; Waldhauser & Ellsworth, 2000; Yoshida & Hasegawa, 2018a, 2018b). On the other hand, some diversity in hypocenter distribution reflects the true nature of fault structures (e.g., Kilb & Rubin, 2002; Ross, Hauksson, et al., 2017, 2019; Xue et al., 2018; Yoshida et al., 2014, 2015). In general, larger earthquakes cause larger stress changes further from the fault plane and trigger more off-fault seismicity. This results in a more complex aftershock distribution. We anticipate that this problem can be avoided, and essential information regarding intraplate stress accumulation and release can be gathered, by examining a moderate-sized (M ~ 5) earthquake in detail.

In this study, therefore, we examine the spatiotemporal distribution of precisely relocated hypocenters of foreshocks and aftershocks and the coseismic slip distribution of the 2017 M5.2 Akita-Daisen earthquake in NE Japan, to shed light on processes that release stress within the plate. Our results indicate that (1) the foreshocks, mainshock, aftershocks, and postseismic slip all released stress at different segments of the intraplate fault within the NE Japan island arc crust, and (2) much like interplate earthquakes, there are possible signs of aseismic phenomena behind the occurrence of this M5 intraplate earthquake.

2. The 2017 M5.2 Akita-Daisen Earthquake

An M5.2 earthquake occurred on 8 September 2017 in Akita-Daisen, a northern part of inland NE Japan (Figure 1), at a depth of about 10 km. This paper refers to the event as the Akita-Daisen earthquake. This earthquake is the largest to have occurred in the northern part of NE Japan since the 2011 M9 Tohoku-Oki earthquake. The focal area is surrounded by the national dense seismic network (supporting information Figure S1a). The moment magnitude and centroid depth listed in the F-net moment tensor catalog (Fukuyama, 1998) is Mw 4.9 and 5 km, respectively.

The hypocenters of 554 seismic events with $M_{\mathrm{JMA}} \geq 1$ are shown in Figures S1b–S1k. They are listed in the Japan Meteorological Agency (JMA) unified catalog for the period from 1 January 2003 to 31 December 2018. Their depths range from 8 to 12 km. They show a cloud-like spatial distribution across a diameter of a few kilometers, and no planar structure can be observed.

Around the focal region, the stress field was estimated to have rotated >90° after the 2011 Tohoku-Oki earthquake, transitioning from a dominantly E-W compressional reverse-fault regime to an NNE-SSW compressional strike-slip fault regime, because of the static stress change (1 MPa of differential stress) caused by the earthquake (Figure 1a). If this is the case, the differential stress magnitude in the region should be less than

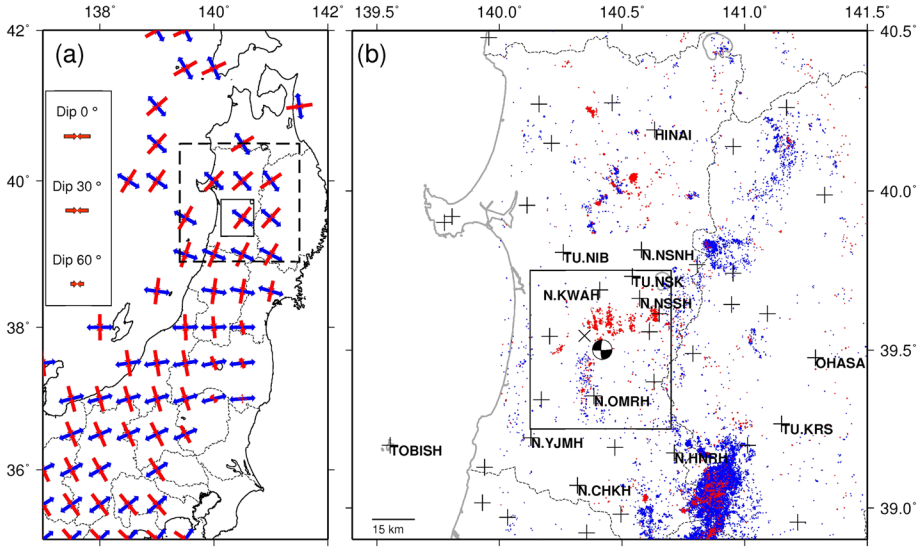

Figure 1. The location of the focal region of the 2017 *M*5.2 Akita-Daisen earthquake. (a) Orientations of the maximum and minimum principal compressional axes of the static stress change of the 2011 *M*9 Tohoku-Oki earthquake are indicated by red and blue bars, respectively. The length of the bar corresponds to the plunge of the principal stress axes. The static stress change was computed by Yoshida et al. (2012) using the coseismic slip model of Iinuma et al. (2011). The broken and solid rectangles indicate the range of the map shown in Figures 1b and 4a, respectively. (b) Hypocenters of earthquakes that occurred before (blue) and after (red) the 2011 Tohoku-Oki earthquake. Plus symbols represent seismic stations. Station names are shown only for stations used for the waveform inversion. The x mark indicates the location of the nearest KiK-net station (AKTH16). The solid rectangle denotes the area shown in Figure 2a. The "beach ball" symbol shows the focal mechanism of the mainshock listed in the F-net catalog.

1 MPa (Yoshida et al., 2012). Subsequent studies, however, have suggested the possibility that the observed stress rotation in this region is the product of heterogeneity in stress fields (Yoshida, Hasegawa, et al., 2019).

The moment tensor solution of the Akita-Daisen earthquake shows a NE-SW compressional strike-slip earthquake, according to the F-net moment tensor catalog, which is consistent with the stress field produced by the 2011 Tohoku-Oki earthquake (Figure 1a). Seismicity drastically increased in and around the focal region of the Akita-Daisen earthquake immediately after the 2011 Tohoku-Oki earthquake (Figure S2). The shear stress magnitude on the fault plane of the Akita-Daisen earthquake increased continuously after the 2011 Tohoku-Oki earthquake occurred (Figure S3) due to postseismic deformation, which probably contributed to the occurrence of the Akita-Daisen earthquake.

3. Methods

3.1. Hypocenter Relocation

We precisely determined the earthquake hypocenters listed in the JMA unified catalog shown in Figure S1a. We followed the procedure outlined in Yoshida and Hasegawa (2018a). We first extracted the P-wave (49,070 picks) and S-wave (47,566 picks) differential arrival time data from the JMA unified catalog. We also used waveform data obtained at stations close to the source area (Figure S1a) for the waveform correlation measurements. The stations are three-component velocity seismometers with a sampling rate of 100 Hz, operated by Tohoku University, JMA, and Hi-net (National Research Institute for Earth Science and Disaster Resilience, 2019a). We applied a band-pass filter of between 5 and 12 Hz and computed the cross-correlation function. Derived differential arrival times were used if the cross-correlation coefficient was higher than 0.8. The number of differential arrival time data for P and S waves, derived from waveform cross-correlation delay measurements, was 175,817 and 204,395, respectively.

We then applied the double-difference earthquake relocation method (Waldhauser & Ellsworth, 2000) to differential arrival time data. We assumed the 1-D velocity model of Hasegawa et al. (1978), which was used routinely at Tohoku University to determine hypocenter locations and focal mechanisms for events in NE

Japan. The residual of the differential arrival times decreased from 82 to 20 ms during processing. We evaluated the uncertainty in the relative hypocenter locations by recalculating the relocations 1,000 times, based on bootstrap resampling of differential arrival time data. The 95% confidence regions of the relative hypocenter locations of close events (<1 km) are 0.0005° in longitude, 0.0003° in latitude, and 224 m in depth on average. This method focuses on estimating relative locations of hypocenters, which is consistent with our goal. For absolute locations, however, the hypocenters determined above might be less reliable than those based on absolute arrival time data. We, therefore, shifted the centroid of relocated hypocenters to the location of the centroid of hypocenters listed in the JMA catalog while maintaining the relative locations.

3.2. Determination of Focal Mechanisms

We used the amplitudes of direct P and S waves (corrected by those of a reference earthquake whose focal mechanism was known) to calculate the focal mechanisms. We followed the procedure outlined in Yoshida, Saito, et al. (2019), which utilizes the amplitude ratios of P, SH, and SV waves by assuming that the medium in the vicinity of the source is homogeneous and isotropic (Dahm, 1996). We limited the distance between target and reference events to less than 3 km. We used the waveform correlation between the target earthquake and a reference earthquake to reliably obtain the amplitude ratio data.

Sixteen focal mechanisms determined and compiled by Yoshida et al. (2012) Yoshida, Hasegawa, et al. (2019) were adopted as reference focal mechanisms. Amplitude ratio was computed at each seismic station if the cross-correlation coefficient is greater than 0.8. If amplitude ratio data were obtained from more than eight different seismic stations, we estimated the moment tensor components. We computed 2,000 focal mechanisms for each target event based on bootstrap resampling of amplitude ratio data. The difference in focal mechanisms from the best solution was measured by the three-dimensional (3-D) rotation angle (Kagan, 1991). If the 90% confidence region was larger than 30°, we discarded the result. Thus, the moment tensor solutions of 273 $M_{\mathrm{JMA}} \geq 1$ events were determined.

3.3. Estimation of Rupture Process

We used seismic waveform data to estimate the coseismic slip distribution of the mainshock. We first removed the site and path effects from the observed waveforms and obtained apparent moment rate functions (AMRFs) of the mainshock using the empirical green function (EGF) method (e.g., Hartzell, 1978). We then inverted the AMRFs for the spatiotemporal distribution of fault slip. The procedure is similar to that of Ross, Kanamori, et al. (2017).

3.3.1. Estimation of Apparent Moment Rate Functions of the Mainshock

We used the iterative time-domain approach developed by Ligorría and Ammon (1999) after Kikuchi and Kanamori (1982) for the deconvolution of waveforms. We used waveforms from the largest *M*3.4 foreshock, which occurred close to the mainshock hypocenter (<350 m according to the relocated hypocenters) as EGF. This earthquake has a similar focal mechanism to the mainshock. We hereafter refer to this earthquake as the "EGF event." Examples of strong waveforms of the mainshock and the EGF event obtained at the nearest KiK-net (National Research Institute for Earth Science and Disaster Resilience, 2019b) station are shown in Figure S4. We only used S waves (transverse components) for the waveform deconvolution because the S/N of the P waves of the EGF event was low at distant stations. The cutoff frequency of the low-pass (Butterworth-type) filter used in the algorithm was set to 3 Hz. If the obtained apparent source time function can explain more than 80% of the observed waveforms in terms of variance reduction, we regarded the deconvolution as successful. Figure 2 shows the AMRFs recorded at 13 different seismic stations. Since the result at the nearest KiK-net station (Figure S4c) does not fit this criterion (only 73.3% was reproduced), this result was not used for the waveform inversion. However, we can see that the characteristics of the AMRF are quite similar to the results with similar direction (e.g., TU.NIB).

Accurate onset times of AMRFs are necessary to accurately estimate the source process. This requires that the arrival time of the mainshock S waves is accurately picked; however, this is difficult when the onset is emergent and contaminated by the P-coda wave. In fact, the onset of P waves implies that slip in the initial stage (~0.1 s) is smaller than slip at the later stage (Figures S5a and S5b), which suggests that the onset of S waves also has a small signal. The waveform of the mainshock in the initial stage (−0.1 to 0.1 s in Figure S5b) is similar to that of the EGF event (Figure S5c). This supports the result that the distance between the

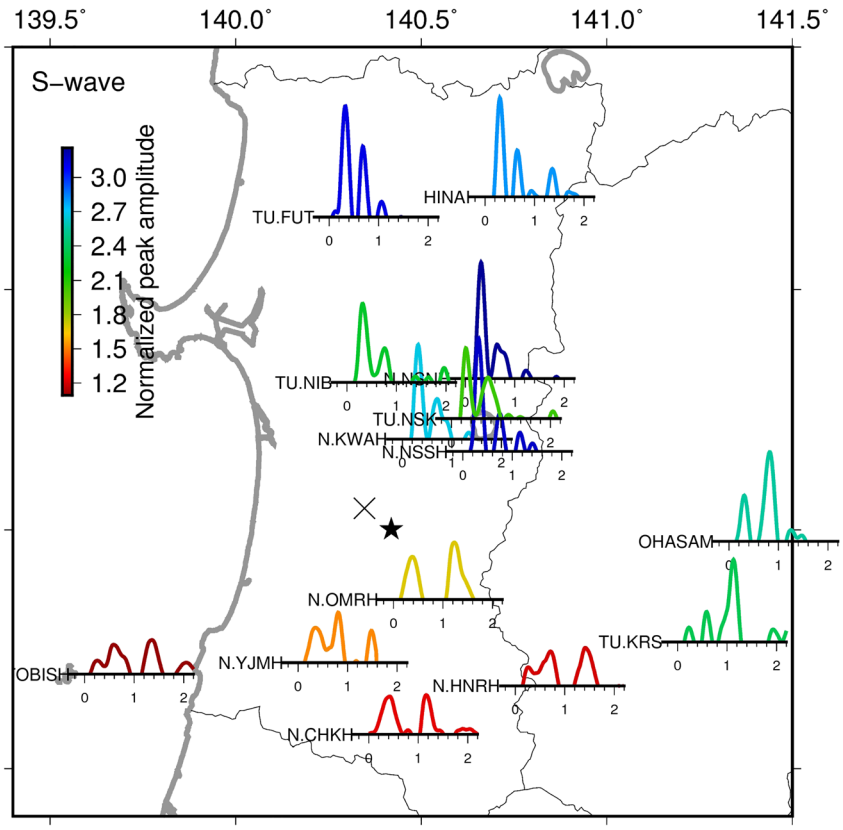

Figure 2. Distribution of AMRFs computed from waveform deconvolution. The functions are plotted at the locations of the seismic stations and colored according to maximum amplitude. Tick marks denote 0.2 s intervals. The black star denotes the location of the mainshock. Timings of AMRFs are aligned such that the onset of all AMRFs occurs at ~0 s. The x mark indicates the location of the nearest KiK-net station (AKTH16).

mainshock and the EGF event was small and may indicate that the mainshock rupture initiated with a similar rupture to that of the EGF event, but finally became larger earthquakes.

We could only pick the onset of the emergent S wave with confidence using data from a limited number of stations. We assumed that V_p/V_s near the hypocenters of the mainshock and the EGF event were uniform, following Shimamura et al. (2011). We then estimated the differential arrival times of S waves between the mainshock and the EGF event at each station based on the obtained arrival time of P and S waves and used these estimates as reference points to pick the onsets of S waves. The relationship between the differential arrival time of P and S waves between the mainshock and the EGF event is shown in Figure 3a. The differential arrival times are concentrated on a line, which corresponds to uniform V_p/V_s. In Figure 3b, we aligned AMRFs by the mainshock S-wave arrival time, thus, obtained. The timing of the second pulse can be observed to correlate well with the azimuth.

3.3.2. Finite Fault Inversion

The AMRFs were inverted to obtain the spatiotemporal distribution of fault slip, following the method of Hartzell and Heaton (1983) and Mori and Hartzell (1990) using the linear equation:

$$d_{\mathrm{obs}} = Gm, \tag{1}$$

where d_{obs} is the data vector containing the AMRFs, G is the matrix of synthetics, and m is the solution vector of the subfault weights. We assumed that the source nucleated at the single point on the fault surface and that slip propagated over the fault plane with a constant rupture velocity V_r. We computed the relative delay times between each source node and a given station using the 1-D model formulated by Hasegawa et al. (1978). The fault geometry is assumed to be rectangular with a fault strike of 0° and a

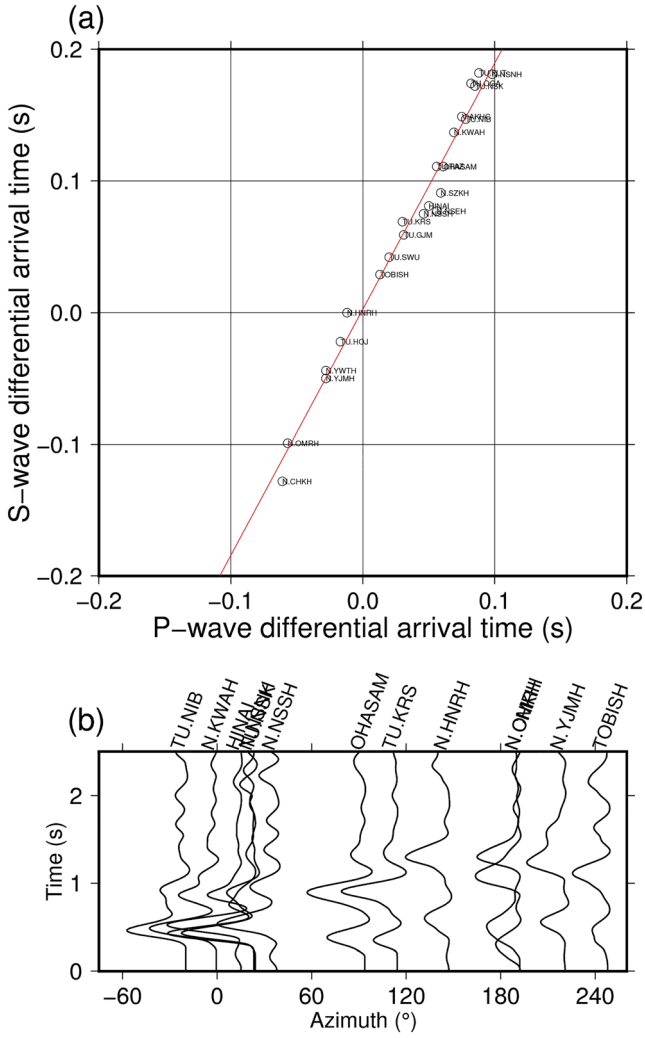

Figure 3. (a) Differential arrival times of P and S waves between the mainshock and the EGF event. The red line indicates the best fit linear relationship between P- and S-wave differential arrival times. (b) AMRFs aligned by the onset of S waves.

dip angle of 80°, based on the mainshock focal mechanism and the hypocenter distribution. We varied V_r/V_s from 0.1 to 0.9, over intervals of 0.1. The length and width of the model fault were set to twice the rupture distance over 2.0 s. The model fault was divided into 31 × 31 subfaults. The length and width of each subfault depend on the assumed value of V_r/V_s. For example, they are 396 m in case of $V_r/V_s = 0.9$.

At individual points on the fault, we represented the local moment rate function as a superposition of five synthetic sub moment rate functions (sMRFs) with different onset timings with regular intervals. The sMRFs were computed by applying the same low-pass filter as that used for the waveform deconvolution to symmetric triangles. The half duration of the triangles and the time intervals between the onset of the five sMRFs were set to t_h. The initiation timing of the first sMRF was set to when the rupture front reaches the center of the subfault. Their amplitudes were determined in the inversion. We assumed t_h to be 0.09 s, which corresponds to two thirds of the time necessary for the rupture front to pass one subfault. We introduced a constant damping factor (λ) and a smoothing factor (e_s) with the same value ($\lambda = e_s = 2$), which was determined based on the trade-off curve (Figure S6), and employed the nonnegative least squares algorithm of Lawson and Hanson (1995) to ensure slip positivity.

Figure S7a shows a comparison of the assumed values of V_r/V_s against the variance reductions VR between the theoretical and observed AMRFs.

$$VR = \sum_{i=1}^{n} \left(1 - \frac{\sum (d_{\mathrm{obs}}(t_i) - s(t_i))^2}{\sum d_{\mathrm{obs}}^2(t_i)} \right), \tag{2}$$

where $d_{\mathrm{obs}}(t_i)$ and $s(t_i)$ are the time series of the observed and synthetic AMRFs, respectively. The best agreement was achieved when $V_r/V_s = 0.9$, with a variance reduction of 84%. This value falls within the typically documented range of 0.6–0.9 (Geller, 1976; Lay et al., 2010). The maximum derived slip amount was 14.6 cm.

However, differences in VR are subtle when $\frac{V_r}{V_s} \geq 0.6$, so we cannot reject the values simply based on the fitting of waveforms. Furthermore, we obtained comparable VR values even if we allowed the values of V_r/V_s to be higher than 1.0 (Figure S7). In fact, the best value of VR was achieved when V_r/V_s was assumed to be 1.1 (VR = 86%). It is possible that the rupture propagates faster than the S-wave velocity for Mode II fractures (Andrews, 1976; Burridge, 1973; Xia et al., 2004), and it may be possible that the rupture of the 2017 Akita-Daisen earthquake was of supershear type. However, the differences in VR were only slight in the interval $0.6 \leq \frac{V_r}{V_s} \leq 1.3$, and a supershear rupture is, at present, considered to be an exception (e.g., Bouchon & Vallée, 2003; Geller, 1976; Lay et al., 2010). Hereafter, we discuss the results of the coseismic slip distribution obtained by assuming $V_r/V_s = 0.9$. Although the assumed value of rupture speed directly affects the spatial extent of the estimated rupture area, the effect is not dramatic in this interval. In section 5.2, we show that coseismic slip distribution is not sensitive to changes in the value of V_r/V_s when it is assumed to be ≥0.6. Furthermore, since differences in the assumed value of t_h affect the resultant coseismic slip distribution only slightly, we hereafter assume $t_h = 0.09$ s.

The measurement error of the initiation timings of P and S waves is a possible cause of the estimation error of the coseismic slip distribution. We examined the uncertainty of the coseismic slip distribution using 1,000 simulated AMRF data sets, produced by fluctuating the initiation timings of AMRFs. The probability distribution of fluctuation is assumed to be a uniformly random distribution ranging from −0.15 to 0.15 s. The frequency distribution of VR of 1,000 results based on the simulated data sets is shown in Figure S8a. The

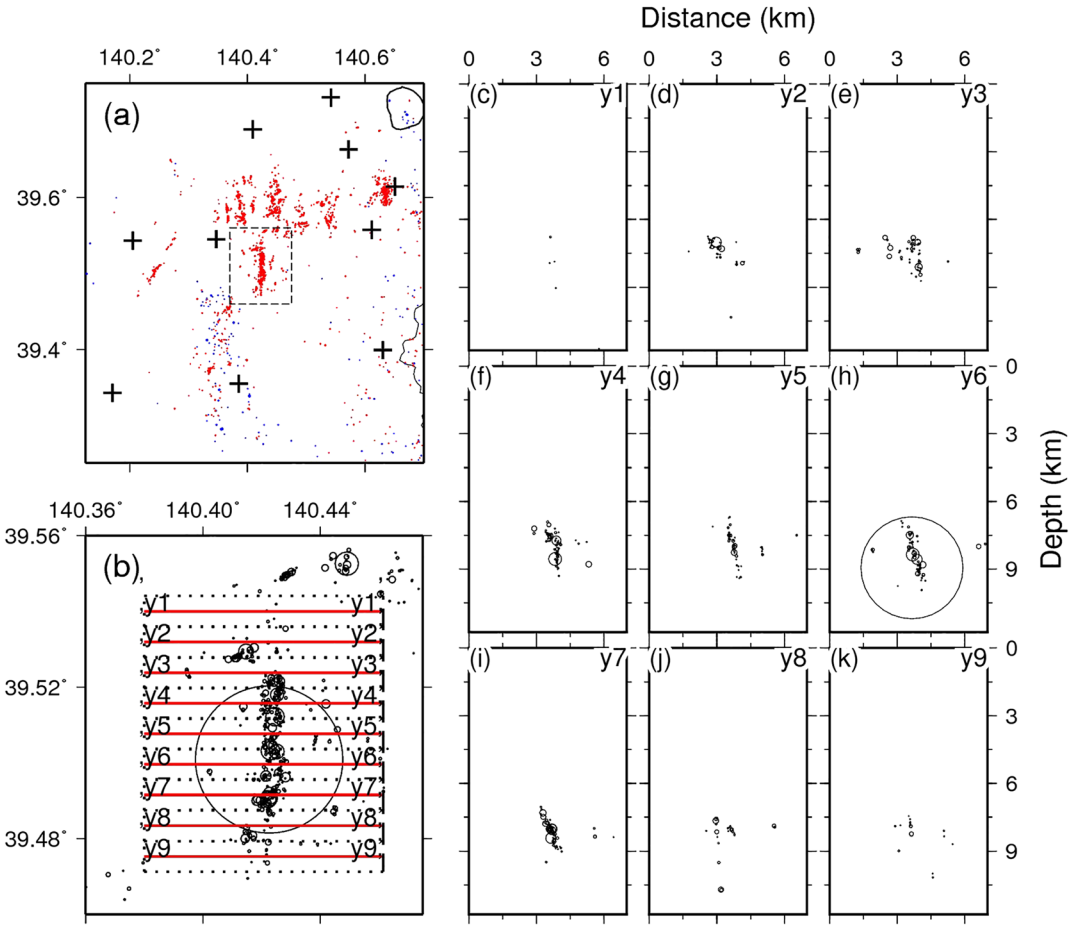

Figure 4. Distribution of the relocated hypocenters. (a) Hypocenters of earthquakes that occurred before (blue) and after (red) the 2011 Tohoku-Oki earthquake. Hypocenters in this region were relocated using the procedure outlined in section 4.1. Plus symbols represent seismic stations. The dashed rectangle denotes the area shown in (b). (b) A map view showing the focal region of the 2017 Akita-Daisen earthquake. (c–k) Cross-sectional views of vertical hypocenter distribution along the lines indicated in (b). Black circles represent hypocenters. The size of each circle corresponds to the diameter of the fault, assuming a stress drop of 3 MPa for illustrating purposes.

mean value and the standard deviation of *VR* are 76.7% and 4.0%, respectively. The mean value is well below that of the main result (84%), justifying the validity of the initiation timings used for the main result in the scale of added noise. The mean coseismic slip distribution and the standard deviation of slip amount at each subfault are presented in Figures S8b and S8c, respectively. We also conducted the waveform inversions by shifting the initiation timings of all the AMRFs all together by the same amount from −0.07 to 0.07 s. The results are shown in Figure S9. The results shown in Figures S8 and S9 are used for the measures of uncertainty of the result.

4. Results

4.1. Fault Structure and Migration Behavior of Foreshock and Aftershock Activities

The distribution of relocated hypocenters is shown in Figure 4 for the same area as Figure S1. Most of the relocated hypocenters are distributed on a single planar structure. Figures 5 and 6 show an enlarged view of the relocated hypocenters and focal mechanisms, respectively.

The planar distribution of the hypocenters is characterized by N-S strike over a length of 5 km and width of 4 km (Figures 4 and 5). Its dip is almost vertical in the northernmost cross sections, while it dips toward the east at an angle of ~65–70° to the south. This geometry is consistent with focal mechanisms in this area (Figure 6), which are characterized by right-lateral strike slip with almost vertical nodal planes in the

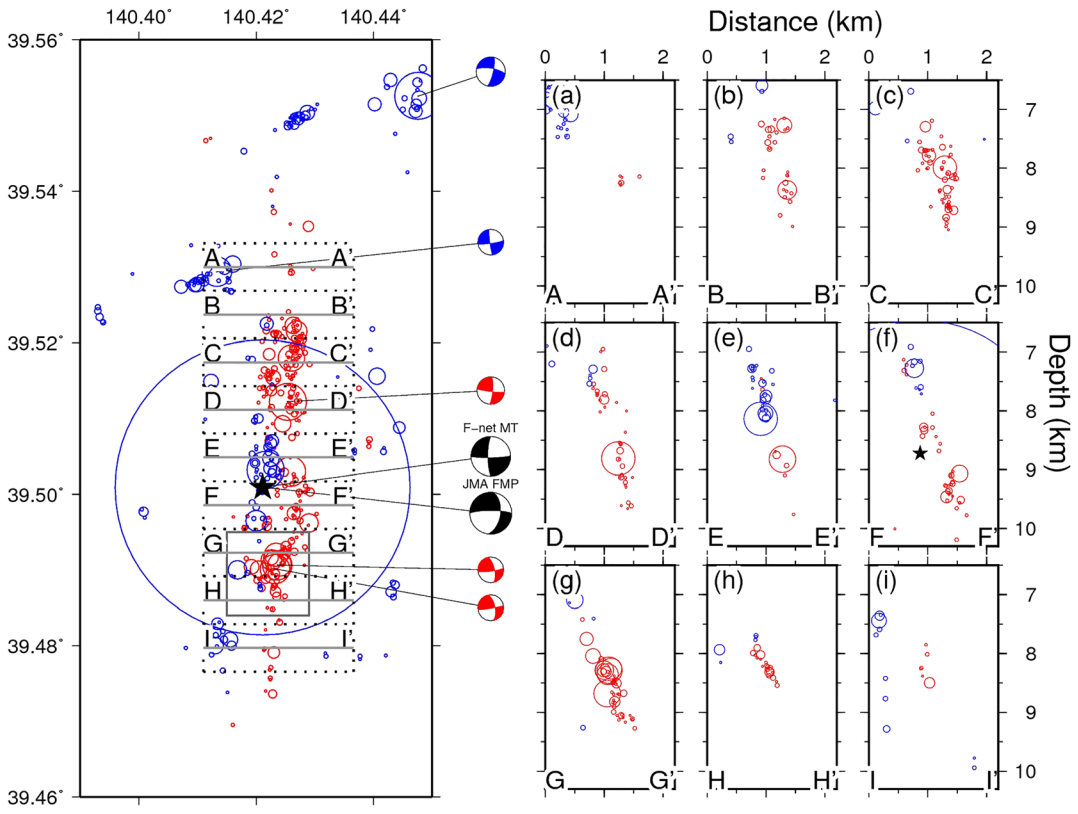

Figure 5. Map and (a–i) cross-sectional views (A–I) showing hypocenters (represented by circles) of earthquakes before (blue) and after (red) the mainshock. The size of each circle corresponds to the fault diameter, assuming a stress drop of 3 MPa for illustrating purposes. Blue and red beach balls show the focal mechanisms derived from the JMA catalog before and after the mainshock. These focal mechanisms were determined from first-motion polarity data. For the mainshock, the first-motion polarity solution listed in the JMA catalog and the moment tensor solution listed in the F-net catalog are shown by black beach balls. The black star denotes the location of the mainshock.

north and nodal planes with similar dip to the hypocenters in the south. These results strongly suggest that individual earthquakes occur on the same macroscopic planar structure.

Two different kinds of focal mechanism are shown for the mainshock in Figure 5: the first-motion polarity solution listed in the JMA catalog, which represents the fault geometry near the hypocenter, and the moment tensor solution listed in the F-net catalog, which represents the average fault geometry in the entire rupture area. The former has a nodal plane that dips strongly (~65–70°) to the east, which is parallel to hypocenter alignment in the south. The latter has an almost vertical nodal plane and is parallel to hypocenter alignment in the north. This suggests that the mainshock rupture was initiated in the southern part of the rupture area, and the largest slip occurred in the northern part. Different characteristics of AMRFs between the northern and southern stations (Figure 2) support this hypothesis. The duration of the first pulse is shorter, the amplitude is higher, and the time interval between the two pulses is shorter (~0.4 s) at the northern stations. The duration of the first pulse is longer, the amplitude is lower, and the time interval between the two pulses is longer (~1.2 s) at the southern stations. This difference suggests that the first pulse is primarily characterized by northward propagation and the second pulse was produced north of the hypocenter.

Foreshocks and aftershocks appear to have caused slip on different segments of the same plane. Hypocenters of foreshocks, including the largest *M*3.4 event that occurred on 9 September 2016, are located near the hypocenter of the mainshock (Cross Section E in Figure 5). In contrast, aftershock hypocenters are not distributed near the mainshock hypocenter. Figure 7 shows a cross section of hypocenters along the fault strike. A clear seismic gap of aftershocks with a length of about 2 km and a width of about 1 km can be observed around the mainshock hypocenter (Figure 7c). This seismic gap may represent large slip regions of the mainshock, as

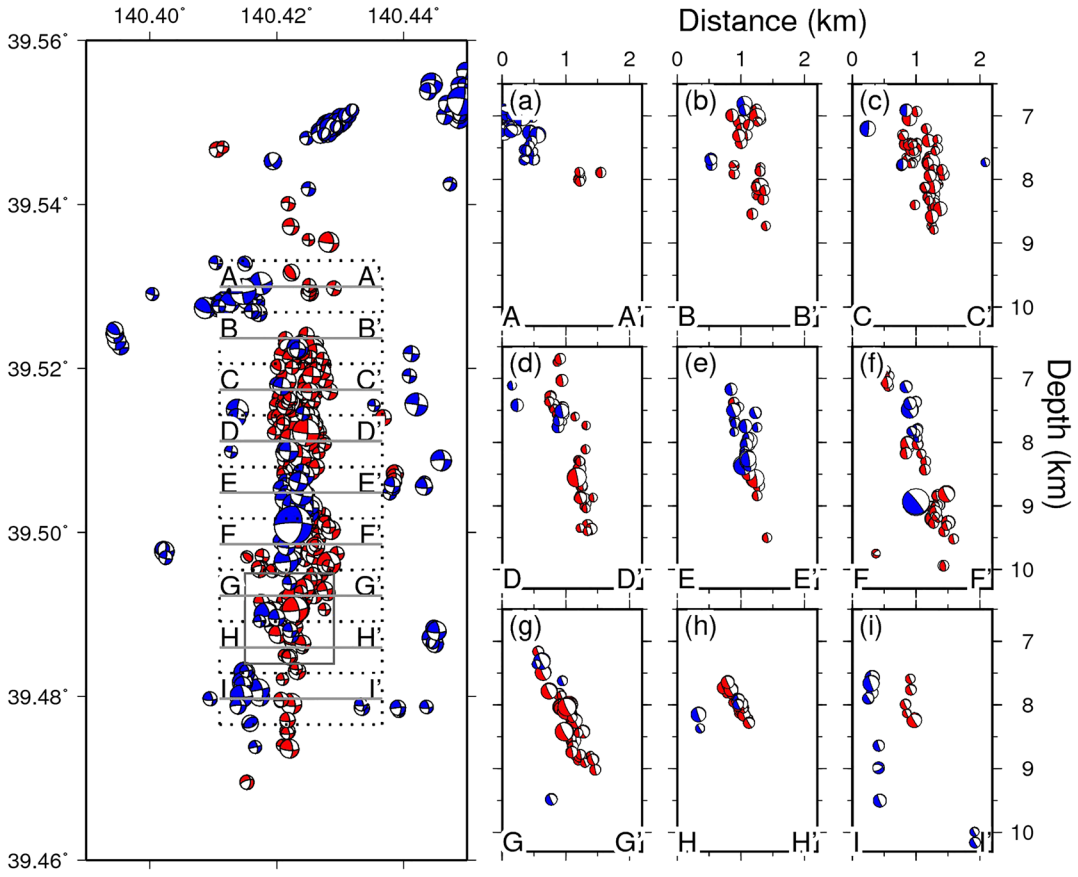

Figure 6. Map and (a–i) cross-sectional views (A–I) of focal mechanisms before (blue) and after (red) the mainshock. Beach balls represent focal mechanisms.

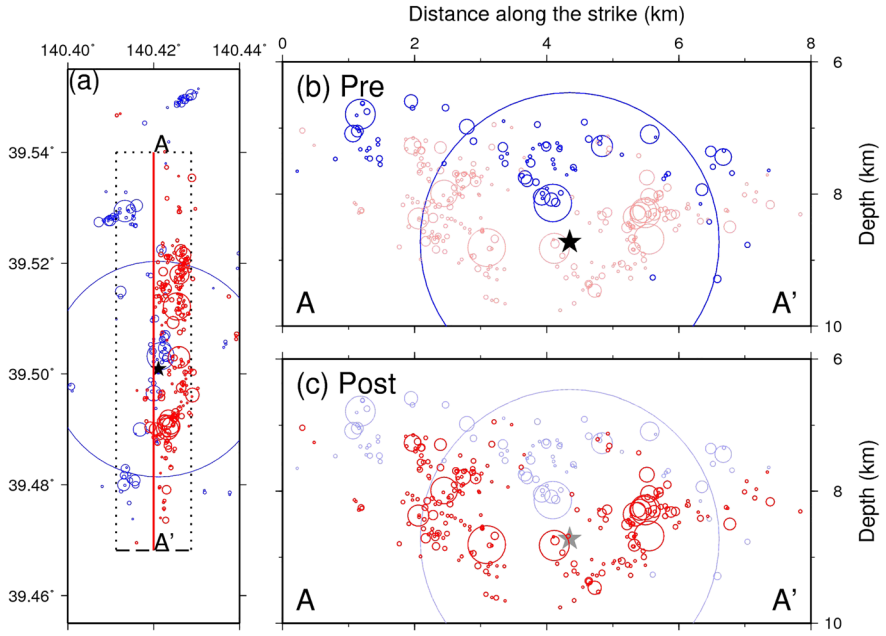

Figure 7. (a) Map view and (b, c) cross-sectional views along the strike of the rupture zone showing hypocenters of earthquakes (represented by circles) before (blue) and after (red) the mainshock. The size of each circle corresponds to the fault diameter, assuming a stress drop of 3 MPa, for illustrating purposes. The black star denotes the location of the mainshock.

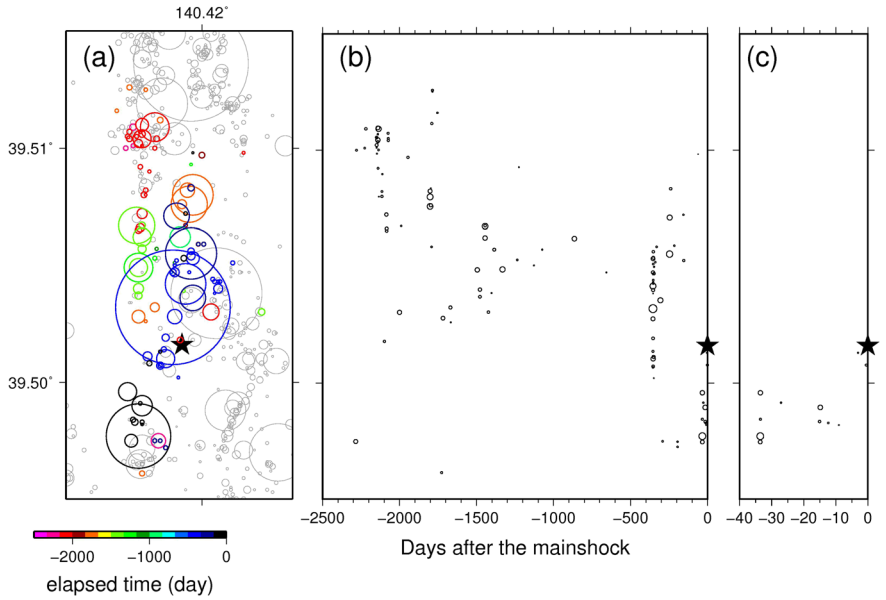

Figure 8. Temporal variations of hypocenters in the foreshock sequence. (a) Foreshock hypocenters are plotted by time of occurrence according to the color scale. (b, c) Time plots of the latitudes of foreshock hypocenters. Circle size represents earthquake magnitude. The black star indicates the location of the mainshock.

reported for larger earthquakes based on the direct comparison of aftershock distribution and coseismic slip distribution (e.g., Asano et al., 2011; Das & Henry, 2003; Ebel & Chambers, 2016; Mendoza & Hartzell, 1988; Ross, Kanamori, et al., 2017; Ross et al., 2018; Wetzler et al., 2018; Woessner et al., 2006; Yoshida, Hasegawa, & Okada, 2016).

Figure 8 shows the time of occurrence of foreshocks near the mainshock hypocenter (<~1 km) with distance along the fault strike from the mainshock hypocenter. The foreshock sequence initiated ~2,000 days before the mainshock, with foreshock hypocenters gradually migrating from north to south. Foreshocks occurred closest to the mainshock hypocenter 1 year before the mainshock, reaching the area south of the mainshock ~30 days before the mainshock took place (Figure 8b). Foreshocks migrated back north before the mainshock occurred (Figure 8c).

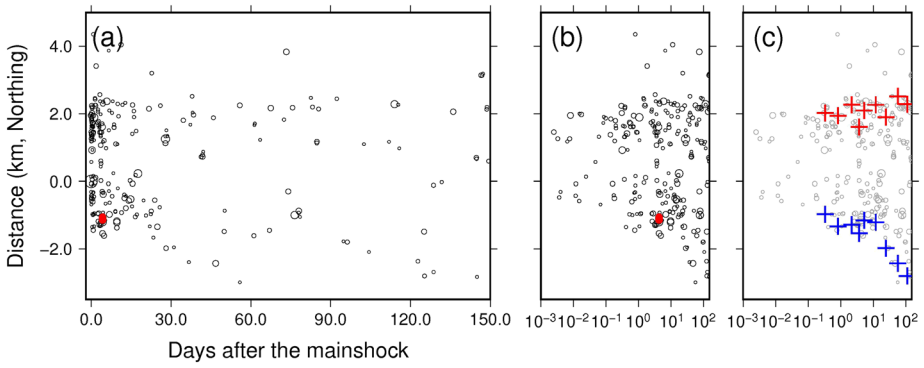

Figure 9. Time plots of along-strike distance of aftershock hypocenters away from the mainshock hypocenter. Circle size indicates earthquake magnitude. Red dots represent possible repeating earthquakes. (a) Distance (km) along the strike as a function of time (days). (b, c) Distance (km) along the strike as a function of the logarithm of time (days). In (c), red and blue crosses represent the values at each bin, above and below which 10% of earthquakes occur, respectively. Each bin has the same number of events.

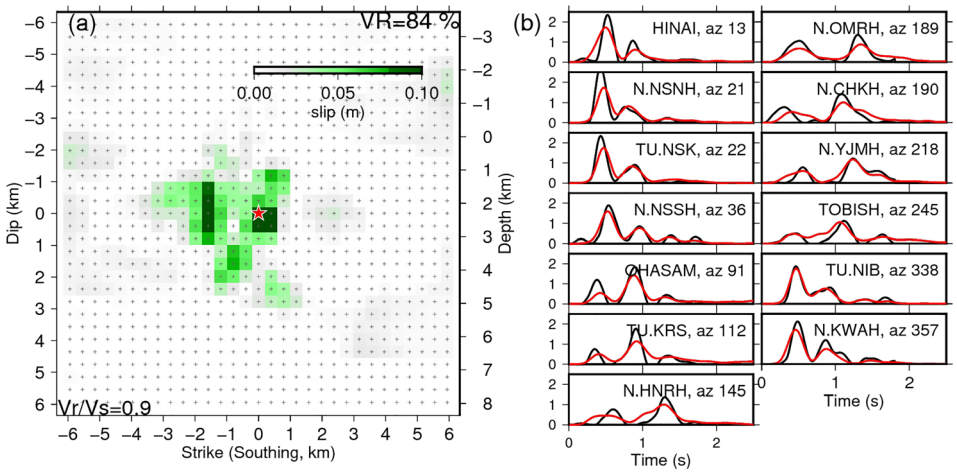

Figure 10. (a) The coseismic slip distribution obtained assuming $V_r/V_s = 0.9$. The slip amount is shown by the color scale. (b) Comparison of the observed (black) and synthetic (red) source time functions at each station.

Figure 9 compares the occurrence timing of aftershocks against the distance along the fault strike. The aftershock area expands with time, especially over the first few days to the southern region. The aftershock region expands approximately with the logarithm of time (Figures 9b and 9c).

4.2. Coseismic Slip Distribution of the 2017 *M*5.2 Akita-Daisen Earthquake and Its Relationship With Foreshock and Aftershock Activity

Figure 10 shows the final coseismic slip distribution of the mainshock and a comparison of the observed (black) and synthetic (red) source time functions at each station. There are two large slip regions: a region near the hypocenter and a region north of the mainshock hypocenter, which is consistent with what would be expected from the azimuthal dependency of the AMRFs. The distance between the two large slip areas is approximately 1.5 km. Similar characteristics were obtained for the mean result of the 1,000 simulated coseismic slip distributions (Figure S8b), and for the results produced by systematically shifting the initiation timings of all the AMRFs (Figure S9); they have two large slip regions near the hypocenter and ~1.5 km north from the hypocenter. Existence of the two slip peaks is significant from the standard deviation of the 1,000 simulated coseismic slip distributions (Figure S8c). These results indicate that the characteristics of the coseismic slip distribution obtained in this study are robust.

Figure 11 compares the coseismic slip distribution with the hypocenter distributions. Aftershocks occurred abundantly outside the edges of the two large slip portions (Figure 11b). The area with a relatively small amount of coseismic slip between two large slip regions corresponds to the deeper extension of intense foreshock activity. Comparisons of the coseismic slip amount against number of foreshocks and aftershocks along the large slip regions are shown in Figures 11c and 11d, respectively. As a whole, the mainshock, foreshocks, and aftershocks cause slip on different parts of fault. This pattern barely changes if other values in the interval $0.6 \leq \frac{V_r}{V_s} \leq 1.3$ are used for the waveform inversion (Figure S10).

The theoretical equations compiled by Okada (1992) were used to calculate the change in background shear stress along the fault. We assumed a homogeneous elastic half-space with a Poisson's ratio of 0.25 and a rigidity of 30 GPa. The average stress drop was 1.4 MPa, which was weighted by the slip amount (Noda et al., 2013; Shao et al., 2012). The largest value was 7.0 MPa near the hypocenter. The results are compared with the locations of foreshocks and aftershocks in Figures 12a and 12b, respectively. Aftershocks tend to occur in locations with positive shear stress. The model results showed that shear stress change was positive for 75% of $M > 2$ events.

We estimated the radiation energy using the method proposed by Vassiliou and Kanamori (1982), which employs the integration of the square of the seismic moment acceleration function. The obtained radiation energy E_R was 4.7×10^{11} J, which follows that the scaled energy $\frac{E_R}{M_o}$ was 1.7×10^{-5}. The assumption of a

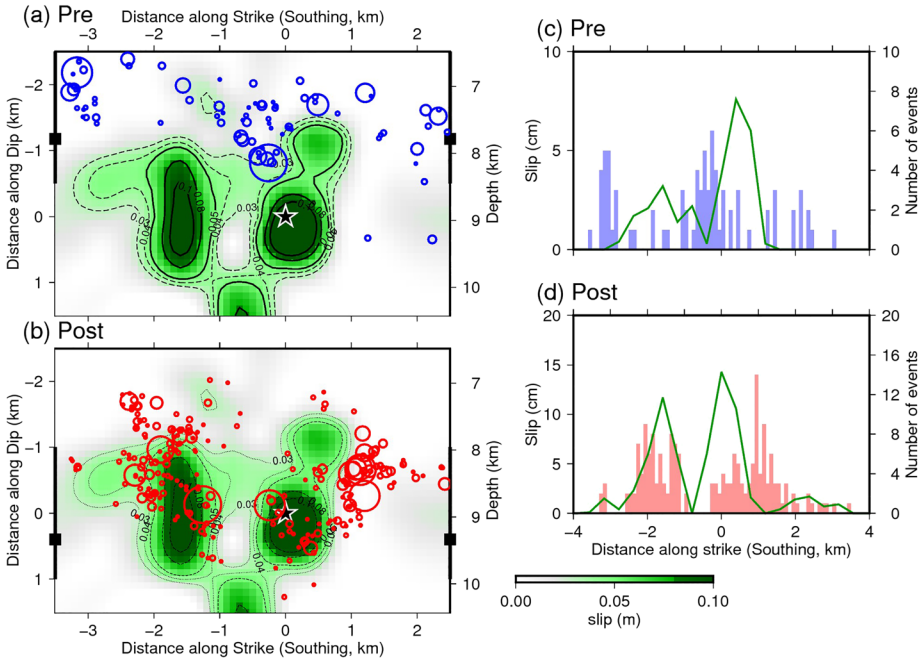

Figure 11. Comparison of the interpolated coseismic slip distribution (green) against (a) foreshock sequences (blue circles) and (b) aftershock sequences (red circles). Along-strike and along-dip distances are measured with respect to the mainshock hypocenter (black star). In (c) and (d), the amount of coseismic slip (green line) is compared with the number of events before and after the mainshock within the along-strike zone shown by the triangles and bold lines in (a) and (b).

rigidity μ of 30 GPa yielded an apparent stress $\sigma_{\mathrm{ap}} = \mu \frac{E_R}{M_o}$ of 0.5 MPa. The radiation efficiency $\eta_R = 2\frac{\mu}{\sigma_E}\left(\frac{E_R}{M_o}\right)$ (Kanamori & Rivera, 2006) was approximately 0.72, which falls in the typical range of Mw > 6.7 earthquakes (Venkataraman & Kanamori, 2004). This value is a few times larger than estimates for recent smaller intraplate earthquakes, such as the 2008 Mw 5.4 Chino Hills, California, earthquake (Shao et al., 2012) and the 2016 Mw 6.2 Tottori earthquake (Ross et al., 2018).

The relatively high radiation efficiency in this study suggests that the Akita-Daisen earthquake occurred on a mature fault. The observation that foreshock and aftershock activities are concentrated on the same planar structure (Figure 5) supports this idea. The relationship between V_r/V_s and η_R is consistent with that of Mode II cracks (Freund, 1972; Venkataraman & Kanamori, 2004).

5. Discussion

5.1. Interpretation of the Results

5.1.1. Foreshock Migration and Aseismic Process Prior to the Mainshock

The migration of foreshocks suggests that aseismic processes, such as aseismic slip and fluid migration, proceeded before the occurrence of the mainshock. Aseismic slip has been detected before the occurrence of large interplate earthquakes (e.g., Ito et al., 2013; Kato et al., 2012; Uchida et al., 2004). For example, the migration of foreshocks toward the rupture initiation point of the mainshock was observed in the 2011 Tohoku-Oki earthquake (Ando & Imanishi, 2011; Kato et al., 2012), which was interpreted as the propagation of aseismic slip. It is possible that such an aseismic slip also contributes to the occurrence of intraplate earthquakes. The hypocenter migration observed for foreshocks near the mainshock hypocenter (Figure 8) might be triggered by the propagation of an aseismic slip.

Another cause of hypocenter migration is the diffusion of fluid. Earthquake swarm activities triggered by the 2011 *M*9 Tohoku-Oki earthquake in inland NE Japan were interpreted to be caused by fluid movement facilitated by the earthquake (Terakawa et al., 2013; Okada et al., 2016; Yoshida & Hasegawa, 2018a, 2018b; Yoshida, Saito, et al., 2019), because their hypocenters exhibited distinct

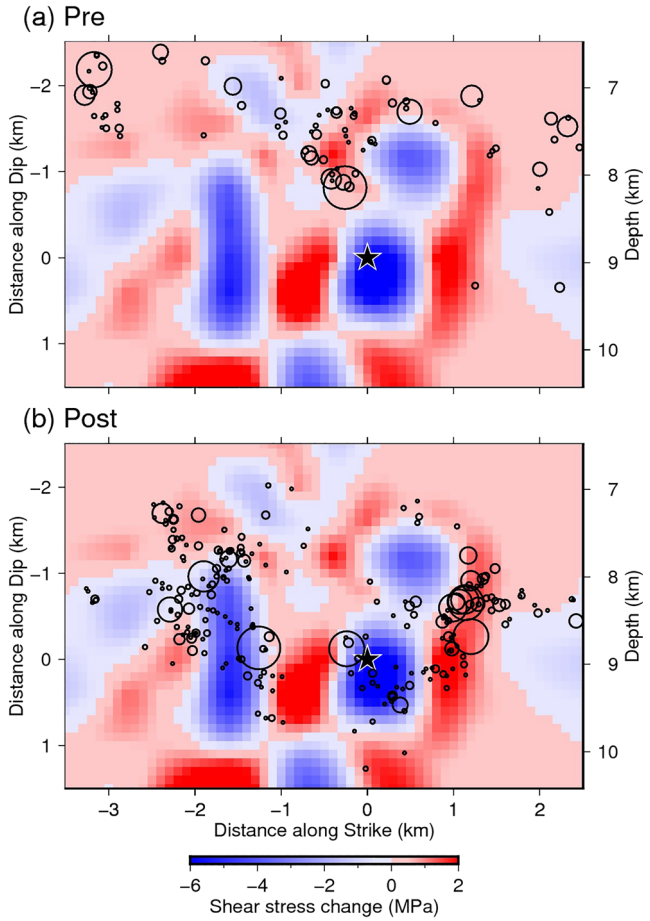

Figure 12. Comparison of the distribution of shear stress change with (a) foreshock sequences and (b) aftershock sequences. Circles show the locations of hypocenters. Along-strike and along-dip distances are measured with respect to the mainshock hypocenter (black star).

migration behaviors upward along several planar structures (Yoshida & Hasegawa, 2018a, 2018b), and seismicity and source parameters exhibited synchronized temporal variations which can be explained by a simple pore pressure diffusion (Yoshida et al., 2016b; Yoshida et al., 2017; Yoshida & Hasegawa, 2018b). The hypocenter migrations observed for these earthquake swarms altogether proceeded to a shallow level, which is different from the present case. However, it is possible that such fluid movement preceded the occurrence of the Akita-Daisen earthquake, which in turn may have affected the frictional properties of the source region, causing the earthquake sequence and aseismic slip.

Quasistatic rupture associated with the nucleation of the mainshock is an alternative mechanism for the occurrence and migration of foreshocks (e.g., Dodge et al., 1996; McGuire et al., 2005; Yabe et al., 2015; Yabe & Ide, 2018). The slip-weakening dependence of frictional strength (e.g., Ida, 1972) predicts that stable slip quasistatically expands with time prior to the dynamic instability that leads to rupture. This feature is confirmed by in situ experiments (Ohnaka & Kuwahara, 1990). Physical simulations indicate that interseismic creep penetrates seismogenic patches from external stable-slip regions before the occurrence of unstable slip (Tse & Rice, 1986).

At present, it is difficult to determine the physics behind the observed hypocenter migration. However, our results suggest that aseismic phenomena preceded the 2017 Akita-Daisen earthquake.

Foreshock activity is sometimes reported to have significantly lower *b* values than regular seismicity (e.g., Nanjo et al., 2012; Suyehiro, 1966; Tormann et al., 2016; Tamaribuchi et al., 2018), which might be related to aseismic processes. In the case of the 2017 Akita-Daisen earthquake, we do not observe a significant change in *b* value. The *b* values of foreshocks and aftershocks are 0.90 and 0.93, respectively (Figure S11). The standard errors for *b* values are 0.13 for both foreshocks and aftershocks according to the solution of Shi and Bolt (1982).

5.1.2. Aftershock Migration and Afterslip Propagation

One possible cause of the expansion of the aftershock region is the propagation of postseismic aseismic slip (e.g., Ariyoshi et al., 2007; Hsu et al., 2006; Kato, 2004; Wesson, 1987). The expansion of aftershock region with the logarithm of time observed in this study (Figure 9) is consistent with observations and simulations of postseismic slip (Frank et al., 2017; Kato, 2007; Peng & Zhao, 2009; Perfettini et al., 2018; Ross et al., 2018). The propagation speed seems lower in the northern front than in the southern front (Figure 9c). The difference in the propagation speed might be related to the difference in effective normal stress and/or frictional properties (Ariyoshi et al., 2007, 2019). Some geodetic studies have showed that moment releases of postseismic slip can be comparable to those of the mainshocks (Freed, 2007; Johanson et al., 2006; Kawasaki et al., 2001; Nishimura et al., 2000; Pritchard & Simons, 2006) especially for small- to moderate-sized earthquakes (Hawthorne et al., 2016). This might suggest that the postseismic slip also plays an important role for the release of stress in the case of this earthquake sequence.

Fluid diffusion is another possible cause for aftershock migration. However, hypocenter fronts expand with the square root of time in fluid diffusion models (e.g., Shapiro et al., 1997), which well describe the expansion of source regions of fluid-injection induced seismicity and many swarm activity in volcanic regions (Parotidis et al., 2003; Yukutake et al., 2011; Shelly, Hill, et al., 2013; Shelly, Moran, et al., 2013; Shelly et al., 2015; Yoshida et al., 2017, 2018). Our observation of aftershock expansion with the logarithm of time is better explained by the postseismic slip propagation model.

Figure 5 shows that several $M \sim 3$ earthquakes occur very close to the southern front of the aftershock area (gray rectangle). Figure 13 shows an enlarged view of the southern portion of the aftershock area.

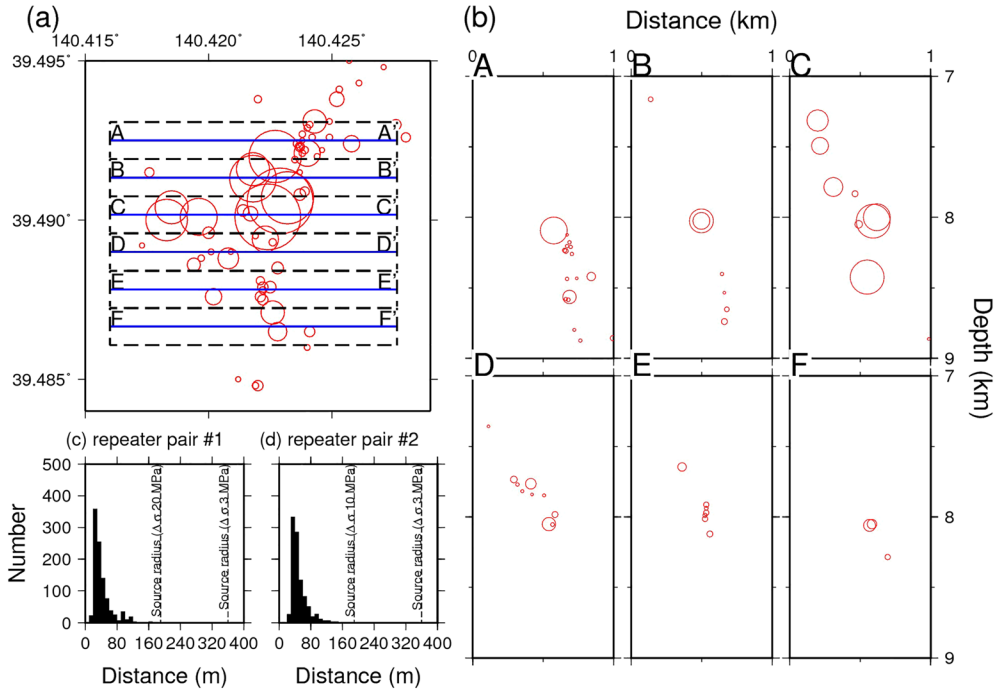

Figure 13. (a) Enlarged map view and (b) cross-sectional views across the fault strike showing the hypocenters of aftershocks (circles). Repeating earthquakes can be observed in Cross Sections B and C. The location is outlined in Figure 5 by the gray rectangle. The size of each circle corresponds to the fault diameter, assuming a stress drop of 20 MPa obtained by Yoshida (2019). (c, d) Uncertainty in the distances between the two sets of possible repeating earthquakes obtained by 1,000 relocation iterations, based on bootstrap subsampling of (c) possible repeating earthquake pair #1 and (d) possible repeating earthquake pair #2.

Two earthquakes of *M*2.6 and *M*2.9 in Cross Section B, at a depth of about 8 km, lie very close to each other (23 m). Similarly, two earthquakes of *M*3.0 and *M*3.2 in Cross Section C, at a depth of about 8 km, are very close to each other (41 m). The earthquakes possibly caused slip on the same portions of the fault. Their distances apart are a few tens of meters, which are much shorter than the fault sizes based on the crack model (360 and 190 m for stress drop of 3 and 20 MPa, respectively). Figures 13c and 13d show the uncertainty in the relative distances of the two possible repeating earthquake pairs obtained by the 1,000 bootstrap hypocenter relocations. In most results, their distances are estimated to be less than 50 m. The locations of these earthquakes are similar but slightly different (a few tens of meters). Example waveforms of these four earthquakes at the nearest seismic station are similar but not identical (Figure S13). The different waveforms suggest that the rupture processes of these earthquakes were quite different. We cannot deny the possibility that these possible repeating earthquakes occurred at slightly different positions (e.g. on conjugate faults). However, such earthquakes occur at the hypocenter expansion front, which suggests the possibility that these are repeating earthquakes caused by postseismic slip propagation.

Mainshock-aftershock sequences are characterized by a decay in the rate of seismicity in proportion to the reciprocal of time (Omori law), and events are often assumed to be triggered by static stress changes from the mainshock (e.g., Dieterich, 1994; King et al., 1994) and/or postseismic slip (e.g., Hsu et al., 2006; Schaff et al., 1998). On the other hand, earthquake swarms, which do not obey the Omori law, are often assumed to be caused by aseismic processes, such as episodic aseismic slip (Chen et al., 2012; Roland & McGuire, 2009; Vidale & Shearer, 2006) or fluid migration (e.g., Hainzl & Ogata, 2005). The number of aftershocks observed after the 2017 Akita-Daisen earthquake follows the Omori law (Figure S12), which suggests that the dominant causes of these aftershocks were static stress change and postseismic slip of the mainshock.

5.1.3. Spatial Separation of Coseismic and Postseismic Slip, and Foreshock and Aftershock Activities

We have suggested that the mainshock, foreshocks, and aftershocks released stress on different segments of the fault. Furthermore, aseismic slip possibly influenced aftershock and foreshock generation, which might also contribute to the redistribution of stress.

According to geodetic estimates, areas that undergo postseismic slip are often spatially separated from those that experience coseismic slip (e.g., Heki et al., 1997; Iinuma et al., 2016; Johanson et al., 2006; Miura et al., 2006; Miyazaki et al., 2004; Wang et al., 2012), which may be attributed to variation in the frictional properties of faults. Fault segments on which postseismic slip occurs are often modeled using velocity-strengthening frictional behavior (e.g., Kato, 2004; Marone, Scholtz & Bilham, 1991; Perfettini & Avouac, 2004; Rice & Gu, 1983; Schaff et al., 1998; Viesca & Dublanchet, 2019). In fact, postseismic slip is often reported to occur at shallower and deeper levels than coseismic slip areas, which can be explained by the dependency of frictional properties on temperature (Blanpied et al., 1995; Tse & Rice, 1986). Postseismic slip sometimes occurs at the same depth as coseismic slip (e.g., Hashimoto et al., 2009; Hearn et al., 2002; Helmstetter & Shaw, 2009; Johanson et al., 2006; Hsu et al., 2006; Miyazaki et al., 2004; Murakami et al., 2006; Pritchard & Simons, 2006; Uchida et al., 2009), which might reflect lateral variations in stress, frictional, and/or rheological properties along faults.

The spatial separation observed in this study may be attributable to differences in frictional properties along the fault; the areas with postseismic slip might have a velocity-strengthening nature but contain some small velocity-weakening patches on which aftershocks occurred. The rupture propagation of the mainshock may have been arrested by such a velocity-strengthening area. We usually do not know whether stable slip occurs along intraplate faults at depth due to the weakness of the geodetic signal. However, the observation that fault segments characterized by velocity strengthening possibly exist may suggest that stable slip proceeds there during the interseismic period and that slip deficit accumulates at other fault segments similar to the processes characteristic of plate boundary faults.

Aftershocks did not occur in the area between the two large slip regions and deeper portions ($z > 10$ km) even if the shear stress magnitude was increased by the mainshock (Figure 12). This may indicate that shear stress was released aseismically there rather than through aftershock generation.

5.1.4. Stress Release Processes Along the Fault of the Akita-Daisen Earthquake

The temporal evolution of stress associated the Akita-Daisen earthquake can be summarized as follows:

1. Shear stress along the fault continuously increased following the 2011 Tohoku-Oki earthquake due to coseismic and postseismic deformation. Seismicity drastically increased in and around the focal region after this earthquake.
2. Foreshocks started to occur ~2,000 days before the mainshock, and their hypocenters migrated along the fault plane from north to south, redistributing shear stress on the fault. We suspect the possibility that aseismic slip was responsible for foreshock activity, which also contributed to the redistribution of stress on the fault.
3. The *M*5.2 mainshock finally occurred 6 years after the 2011 Tohoku-Oki earthquake and primary propagated toward the north. The mainshock released shear stress accumulated on some segments of the fault (stress drop of 1.4 MPa on average). The amount of coseismic slip was smaller in areas where foreshocks had already released stress. Heterogeneous states of stress and/or friction may have contributed to the heterogeneous distribution of coseismic slip. The mainshock increased shear stress near the edges of large slip regions.
4. Aftershocks occurred abundantly in areas where shear stress was increased by the mainshock. The aftershock region expanded along the fault strike, associated with the propagation of postseismic slip.

5.2. Implications of the Results

5.2.1. Stress Release Process Along Intraplate Fault

The 2017 *M*5.2 Akita-Daisen earthquake sequence occurred on an intraplate fault within the island arc crust but has similar features to interplate earthquakes. For example, in the case of the 2011 *M*9 Tohoku-Oki earthquake, the spatial distribution of aftershocks shows a clear seismic gap corresponding to the large mainshock coseismic slip region (e.g., Asano et al., 2011; Kato & Igarashi, 2012; Nakamura et al., 2016). Foreshock hypocenters migrated to the rupture initiation point of the mainshock, which was interpreted

as the propagation of aseismic slip (Ando & Imanishi, 2011; Kato et al., 2012). The aftershock region expanded with the logarithm of time, which was attributed to postseismic aseismic slip of the mainshock (Lengliné et al., 2012; Perfettini et al., 2018). During the postseismic period, earthquakes repeatedly occurred on the same portions of the fault and were probably triggered by aseismic slip (Uchida & Matsuzawa, 2013). Overall, the foreshocks, mainshock, aftershocks, and postseismic slip all released stress at different fault segments in the *M*9 event (Hasegawa & Yoshida, 2015; Iinuma et al., 2016). These features of the megathrust earthquake are similar to those observed for the *M*5 intraplate earthquake in this study. These similarities are consistent with the hypothesis that the process of stress release along intraplate faults is essentially the same as that along plate boundaries.

In this study, we focused on an *M*5 earthquake sequence that occurred on a single fault plane. Fault structures inside the plate, however, are usually more complex, and their interactions play important roles in the 3-D release of intraplate stress (Urata et al., 2017). When faults are randomly distributed in space, shear strain energy density can be a measure of the average shear stress over the faults (Saito et al., 2018). Recent studies reported that the change of shear strain energy density affects seismicity in the seismogenic zone (Noda et al., 2020). To improve our understanding of the deformation process within the plate, future work should consider the interactions of complex fault distributions.

5.2.2. Constraints on Absolute Stress Magnitude in NE Japan

Drastic changes in focal mechanisms were observed after the 2011 *M*9 Tohoku-Oki earthquake across a large part of east Japan, from the offshore source region (Asano et al., 2011) to inland areas a few hundred kilometers from the source region (Kato et al., 2011; Yoshida et al., 2012). Stress fields were estimated to have rotated by >30° after this earthquake (e.g., Hasegawa et al., 2011, 2012; Hardebeck, 2012; Yoshida et al., 2012). Differential stress magnitudes estimated from the rotation of stress fields are about 20 MPa near the source region (Hasegawa et al., 2012) and as small as 1 MPa in and around the source region of the Akita-Daisen earthquake (Yoshida et al., 2012). This suggests that fault-weakening mechanisms, such as drastic increases in pore pressure, play important roles in the occurrence of earthquakes (e.g., Rice, 1992; Sibson, 1992). On the other hand, stress orientations estimated by seismological methods can be biased due to the existence of strong heterogeneity in stress fields, which can lead to a large underestimation of deviatoric stress magnitudes (Smith & Dieterich, 2010; Smith & Heaton, 2011). To improve our understanding of deformation processes in the Earth, it is important to confirm whether earthquakes occur under such very low shear stresses or not. The source process of the *M*5.2 earthquake provides a clue as to whether the absolute stress magnitude in NE Japan is truly very small (<1 MPa) and whether strength reduction mechanisms are controlling factors for the occurrence of earthquakes.

Earthquakes occur to release strain energy stored in the Earth. The change in strain energy associated with a stress drop of $\Delta\sigma$ is

$$\Delta E = -\frac{M_0}{2\mu}(2\tau_0 - \Delta\sigma), \tag{3}$$

where τ_0 is initial stress (e.g., Aki & Richards, 2002). The radiation energy is a part of the released strain energy, so $-\Delta E > E_r$. Therefore,

$$\tau_0 > \frac{\Delta\sigma}{2} + \mu\frac{E_r}{M_o} = \frac{\Delta\sigma}{2} + \sigma_{\mathrm{ap}}. \tag{4}$$

This relationship is valid regardless of assumptions regarding frictional constitutive laws. If we substitute $\Delta\tau$ = 1.4 MPa and σ_{ap} = 0.5 MPa, we obtain τ_0> 1.2 MPa. Moreover, the stress drop is underestimated if the short-wavelength components are underestimated in the slip distribution (Saito & Noda, 2020). In this case, the initial stress required to excite the earthquake faulting would be larger. Therefore, the initial stress must be larger than 1.2 MPa. This is significantly higher than the 0.5 MPa maximum shear stress magnitude that can reproduce the observed rotations of the principal stress orientations after the 2011 Tohoku-Oki earthquake (Yoshida et al., 2012). The rupture process of the 2017 *M*5.2 Akita-Daisen earthquake, therefore, indicates that the stress orientations in inland NE Japan did not rotate after the 2011 Tohoku-Oki earthquake. The apparent stress rotation probably comes from spatial heterogeneity in the stress fields

(Yoshida, Hasegawa, et al., 2019). This was partly supported by a relatively high radiation efficiency of this earthquake, which suggests that the fault, which caused the 2017 *M*5.2 earthquake, may have slipped repeatedly, and its stress field remains constant for time periods longer than the 6 years, which have elapsed since the 2011 Tohoku-Oki earthquake.

6. Conclusions

Stress accumulation and release processes inside the plate are poorly understood compared to those at plate boundaries. The weakness of the geodetic signal of aseismic slip at intraplate faults and the complexity of fault structure inside the plate restrict our understanding. This study examined foreshock and aftershock activities of the 2017 *M*5.2 Akita-Daisen earthquake, which has a simple fault geometry, to extract information about the processes of stress accumulation and release inside the plate.

We relocated the hypocenters of 554 $M_{JMA} \geq 1$ earthquakes for the period 2003–2018 in the rupture area of the *M*5.2 mainshock using the waveform cross-correlation technique and determined their focal mechanisms. We also determined the moment rate function of the mainshock and estimated the source process based on the waveform inversion method.

Relocated hypocenters indicated that hypocenters were concentrated on a planar structure with N-S strike, which dips eastward at a high angle, consistent with their focal mechanisms. Furthermore, foreshocks, the mainshock, and aftershocks occurred on different fault segments and released stress in a complementary manner.

Hypocenters of foreshocks migrated from the northern to the southern part of the rupture area, which suggests the possibility that the *M*5.2 earthquake and aftershocks were triggered by aseismic phenomena, such as fluid migration and episodic aseismic slip. Foreshock migration may be caused by the quasistatic expansion of stable slip associated with nucleation of the mainshock.

Abundant aftershocks occurred near the edge of large coseismic slip regions, on which shear stress increased after the earthquake. The aftershock region expanded along the fault strike with the logarithm of time, which might be attributed to postseismic aseismic slip of the mainshock. During the postseismic period, possible repeating earthquakes (~*M*3) occurred on the same portions of the fault, which might be triggered by aseismic slip.

Areas with coseismic slip are spatially separated from those with postseismic slip (estimated from aftershock migration), which might reflect differences in frictional properties. The areas with postseismic slip may be of a velocity-strengthening nature but contain some small velocity-weakening patches on which aftershocks occurred. Rupture propagation of the mainshock may have been inhibited by velocity-strengthening areas. This suggests that some portions of the fault creep during the interseismic period. These features are similar to those of megathrust earthquakes, which suggests that the stress release processes along intraplate faults are not essentially different from those along plate boundaries.

Acknowledgments
We deeply thank the editor (Martha Savage), an associate editor, and three anonymous reviewers for their constructive comments, which helped to improve the manuscript. K. Y. thanks Akira Hasegawa for discussions about repeating earthquakes and postseismic slip and Hisahiko Kubo for discussions about waveform inversion. This study used hypocenters and P- and S-wave arrival time data reported in the unified catalog of the JMA (https://www.data.jma.go.jp/svd/eqev/data/bulletin/index_e.html). The seismograms were collected and stored by JMA, national universities, and National Research Institute for Earth Science and Disaster Resilience (http://www.hinet.bosai.go.jp/?LANG=en). The figures in this paper were created using GMT (Wessel & Smith, 1998). This research was supported by the Japan Society for the Promotion of Science (JSPS) KAKENHI Grant JP 17K1437. Obtained results of hypocenters, focal mechanisms, and coseismic slip distribution are available at the website (http://www.aob.gp.tohoku.ac.jp/~yoshida/pub/JGR2020/).

References

Aki, K., & Richards, P. G. (2002). *Quantitative seismology*. Sausalito, California: University Science Books. https://doi.org/10.1016/S0065-230X(09)04001-9

Ando, R., & Imanishi, K. (2011). Possibility of M_w 9.0 mainshock triggered by diffusional propagation of after-slip from M_w 7.3 foreshock. *Earth, Planets and Space*, *63*(7), 767–771. https://doi.org/10.5047/eps.2011.05.016

Ando, R., Nakata, R., & Hori, T. (2010). A slip pulse model with fault heterogeneity for low-frequency earthquakes and tremor along plate interfaces. *Geophysical Research Letters*, *37*, L10310. https://doi.org/10.1029/2010GL043056

Andrews, D. J. (1976). Rupture velocity of plane strain shear cracks. *Journal of Geophysical Research*, *81*(32), 5679–5687.

Ariyoshi, K., Ampuero, J.-P., Bürgmann, R., Matsuzawa, T., Hasegawa, A., Hino, R., & Hori, T. (2019). Quantitative relationship between aseismic slip propagation speed and frictional properties. *Tectonophysics*, *767*, 128,151.

Ariyoshi, K., Matsuzawa, T., & Hasegawa, A. (2007). The key frictional parameters controlling spatial variations in the speed of postseismic-slip propagation on a subduction plate boundary. *Earth and Planetary Science Letters*, *256*(1–2), 136–146.

Asano, Y., Saito, T., Ito, Y., Shiomi, K., Hirose, H., Matsumoto, T., et al. (2011). Spatial distribution and focal mechanisms of aftershocks of the 2011 off the Pacific coast of Tohoku earthquake. *Earth, Planets and Space*, *63*(7), 29.

Asanuma, H., Ishimoto, M., Jones, R. H., Phillips, W. S., & Niitsuma, H. (2001). A variation of the collapsing method to delineate structures inside a microseismic cloud. *Bulletin of the Seismological Society of America*, *91*(1), 154–160. https://doi.org/10.1785/0120000063

Beroza, G. C., & Ide, S. (2011). Slow earthquakes and nonvolcanic tremor. *Annual Review of Earth and Planetary Sciences*, *39*, 271–296.

Blanpied, M. L., Lockner, D. A., & Byerlee, J. D. (1995). Frictional slip of granite at hydrothermal conditions. *Journal of Geophysical Research*, *100*(B7), 13,045–13,064.

Bouchon, M., & Vallée, M. (2003). Observation of long supershear rupture during the magnitude 8.1 Kunlunshan earthquake. *Science*, *301*(5634), 824–826. https://doi.org/10.1126/science.1086832

Burridge, R. (1973). Admissible speeds for plane-strain self-similar shear cracks with friction but lacking cohesion. *Geophysical Journal International*, *35*(4), 439–455.

Chen, X., Shearer, P. M., & Abercrombie, R. E. (2012). Spatial migration of earthquakes within seismic clusters in Southern California: Evidence for fluid diffusion. *Journal of Geophysical Research*, *117*, B04301. https://doi.org/10.1029/2011JB008973

Dahm, T. (1996). Relative moment tensor inversion based on ray theory: Theory and synthetic tests. *Geophysical Journal International*, *124*(1), 245–257.

Das, S., & Henry, C. (2003). Spatial relation between main earthquake slip and its aftershock distribution. *Reviews of Geophysics*, *41*(3), 1013. https://doi.org/10.1029/2002RG000119

Dieterich, J. (1994). A constitutive law for rate of earthquake production and its application to earthquake clustering. *Journal of Geophysical Research*, *99*(B2), 2601–2618. https://doi.org/10.1029/93JB02581

Dodge, D. A., Beroza, G. C., & Ellsworth, W. L. (1996). Detailed observations of California foreshock sequences: Implications for the earthquake initiation process. *Journal of Geophysical Research*, *101*(B10), 22,371–22,392.

Ebel, J. E., & Chambers, D. W. (2016). Using the locations of $M \geq 4$ earthquakes to delineate the extents of the ruptures of past major earthquakes. *Geophysical Supplements to the Monthly Notices of the Royal Astronomical Society*, *207*(2), 862–875.

Frank, W. B., Poli, P., & Perfettini, H. (2017). Mapping the rheology of the Central Chile subduction zone with aftershocks. *Geophysical Research Letters*, *44*, 5374–5382. https://doi.org/10.1002/2016GL072288

Freed, A. M. (2007). Afterslip (and only afterslip) following the 2004 Parkfield, California, earthquake. *Geophysical Research Letters*, *34*(6).

Freund, L. B. (1972). Crack propagation in an elastic solid subjected to general loading—I. Constant rate of extension. *Journal of the Mechanics and Physics of Solids*, *20*(3), 129–140.

Fukuyama, E. (1998). Automated seismic moment tensor determination by using on-line broadband seismic waveforms. *Zisin*, *2*(51), 149–156.

Geller, R. J. (1976). Scaling relations for earthquake source parameters and magnitudes. *Bulletin of the Seismological Society of America*, *66*.

Hainzl, S., & Ogata, Y. (2005). Detecting fluid signals in seismicity data through statistical earthquake modeling. *Journal of Geophysical Research*, *110*, B05S07. https://doi.org/10.1029/2004JB003247

Hardebeck, J. L. (2012). Coseismic and postseismic stress rotations due to great subduction zone earthquakes. *Geophysical Research Letters*, *39*(21), 1–6. https://doi.org/10.1029/2012GL053438

Hartzell, B. Y. S. H., & Heaton, T. H. (1983). Inversion of strong ground motion and teleseismic waveform data for the fault rupture history of the 1979 Imperial Valley, California, earthquake. *Bulletin of the Seismological Society of America*, *73*(6), 1553–1583.

Hartzell, S. H. (1978). Earthquakes aftershocks as Green's functions. *Geophysical Research Letters*, *5*(1), 1–4. https://doi.org/10.1029/GL005i001p00001

Hasegawa, A., Umino, N., & Takagi, A. (1978). Double-planed structure of the deep seismic zone in the northeastern Japan arc. *Tectonophysics*, *47*(1–2), 43–58. https://doi.org/10.1016/0040-1951(78)90150-6

Hasegawa, A., & Yoshida, K. (2015). Preceding seismic activity and slow slip events in the source area of the 2011 Mw 9.0 Tohoku-Oki earthquake: a review. *Geoscience Letters*, *2*(1). https://doi.org/10.1186/s40562-015-0025-0

Hasegawa, A., Yoshida, K., & Okada, T. (2011). Nearly complete stress drop in the 2011 M w 9.0 off the Pacific coast of Tohoku Earthquake. *Earth, Planets and Space*, *63*(7), 703–707. https://doi.org/10.5047/eps.2011.06.007

Hasegawa, A., Yoshida, K., Asano, Y., Okada, T., Iinuma, T., & Ito, Y. (2012). Change in stress field after the 2011 great Tohoku-Oki earthquake. *Earth and Planetary Science Letters*, *355-356*, 231–243. https://doi.org/10.1016/j.epsl.2012.08.042

Hashimoto, C., Noda, A., Sagiya, T., & Matsu'ura, M. (2009). Interplate seismogenic zones along the Kuril–Japan trench inferred from GPS data inversion. *Nature Geoscience*, *2*(2), 141.

Hawthorne, J. C., Simons, M., & Ampuero, J.-P. (2016). Estimates of aseismic slip associated with small earthquakes near San Juan Bautista, CA. *Journal of Geophysical Research: Solid Earth*, *121*, 8254–8275. https://doi.org/10.1002/2016JB013120

Hearn, E. H., Bürgmann, R., & Reilinger, R. E. (2002). Dynamics of Izmit earthquake postseismic deformation and loading of the Duzce earthquake hypocenter. *Bulletin of the Seismological Society of America*, *92*(1), 172–193.

Heki, K., Miyazaki, S., & Tsuji, H. (1997). Silent fault slip following an interplate thrust earthquake at the Japan Trench. *Nature*, *386*(6625), 595.

Helmstetter, A., & Shaw, B. E. (2009). Afterslip and aftershocks in the rate-and-state friction law. *Journal of Geophysical Research*, *114*, B01308. https://doi.org/10.1029/2007JB005077

Hirose, H., Hirahara, K., Kimata, F., Fujii, N., & Miyazaki, S. (1999). A slow thrust slip event following the two 1996 Hyuganada earthquakes beneath the Bungo Channel, southwest Japan. *Geophysical Research Letters*, *26*(21), 3237–3240.

Hsu, Y. J., Simons, M., Avouac, J. P., Galeteka, J., Sieh, K., Chlieh, M., et al. (2006). Frictional afterslip following the 2005 Nias-Simeulue earthquake, Sumatra. *Science*, *312*(5782), 1921–1926. https://doi.org/10.1126/science.1126960

Ida, Y. (1972). Cohesive force across the tip of a longitudinal-shear crack and Griffith's specific surface energy. *Journal of Geophysical Research*, *77*(20), 3796–3805.

Ide, S., Beroza, G. C., Shelly, D. R., & Uchide, T. (2007). A scaling law for slow earthquakes. *Nature*, *447*(7140), 76–79. https://doi.org/10.1038/nature05780

Iinuma, T., Hino, R., Uchida, N., Nakamura, W., Kido, M., Osada, Y., & Miura, S. (2016). Seafloor observations indicate spatial separation of coseismic and postseismic slips in the 2011 Tohoku earthquake. *Nature Communications*, *7*, 13,506.

Iinuma, T., Ohzono, M., Ohta, Y., & Miura, S. (2011). Coseismic slip distribution of the 2011 off the Pacific coast of Tohoku Earthquake (*M* 9.0) estimated based on GPS data—Was the asperity in Miyagi-oki ruptured? *Earth, Planets and Space*, *63*(7), 24.

Iio, Y., Sagiya, T., Kobayashi, Y., & Shiozaki, I. (2002). Water-weakened lower crust and its role in the concentrated deformation in the Japanese Islands. *Earth and Planetary Science Letters*, *203*(1), 245–253.

Ito, Y., Hino, R., Kido, M., Fujimoto, H., Osada, Y., Inazu, D., et al. (2013). Episodic slow slip events in the Japan subduction zone before the 2011 Tohoku-Oki earthquake. *Tectonophysics*, *600*, 14–26.

Johanson, I. A., Fielding, E. J., Rolandone, F., & Bürgmann, R. (2006). Coseismic and postseismic slip of the 2004 Parkfield earthquake from space-geodetic data. *Bulletin of the Seismological Society of America*, *96*(4B), S269–S282.

Kagan, Y. Y. (1991). 3-D rotation of double-couple earthquake sources. *Geophysical Journal International*, *106*(3), 709–716.

Kanamori, H., & Rivera, L. (2006). *Energy partitioning during an earthquake*. Washington, DC: American Geophysical Union.

Kato, A., & Igarashi, T. (2012). Regional extent of the large coseismic slip zone of the 2011 Mw 9.0 Tohoku-Oki earthquake delineated by on-fault aftershocks. *Geophysical Research Letters*, *39*, L15301. https://doi.org/10.1029/2012GL052220

Kato, A., Obara, K., Igarashi, T., Tsuruoka, H., Nakagawa, S., & Hirata, N. (2012). Propagation of slow slip leading up to the 2011 M_w 9.0 Tohoku-Oki earthquake. *Science*, *335*(6069), 705–708. https://doi.org/10.1126/science.1215141

Kato, A., Sakai, S., & Obara, K. (2011). A normal-faulting seismic sequence triggered by the 2011 off the Pacific coast of Tohoku earthquake: Wholesale stress regime changes in the upper plate. *Earth, Planets and Space*, *63*(7), 745–748. https://doi.org/10.5047/eps.2011.06.014

Kato, N. (2004). Interaction of slip on asperities: Numerical simulation of seismic cycles on a two-dimensional planar fault with nonuniform frictional property. *Journal of Geophysical Research*, *109*, B12306. https://doi.org/10.1029/2004JB003001

Kato, N. (2007). Expansion of aftershock areas caused by propagating post-seismic sliding. *Geophysical Journal International*, *168*(2), 797–808.

Kawasaki, I., Asai, Y., & Tamura, Y. (2001). Space–time distribution of interplate moment release including slow earthquakes and the seismo-geodetic coupling in the Sanriku-oki region along the Japan trench. *Tectonophysics*, *330*, 267–283. https://doi.org/10.1016/S0040-1951(00)00245-6

Kikuchi, M., & Kanamori, H. (1982). Inversion of complex body waves. *Bulletin of the Seismological Society of America*, *72*(2), 491–506.

Kilb, D., & Rubin, A. M. (2002). Implications of diverse fault orientations imaged in relocated aftershocks of the Mount Lewis, M_L 5.7, California, earthquake. *Journal of Geophysical Research*, *107*(B11), 2294. https://doi.org/10.1029/2001jb000149

King, G. C. P., Stein, R. S., & Lin, J. (1994). Static stress changes and the triggering of earthquakes. *Bulletin of the Seismological Society of America*, *84*(3), 935–953.

Knopoff, L. (1958). Energy release in earthquakes. *Geophysical Journal of the Royal Astronomical Society*, *1*(1), 44–52. https://doi.org/10.1111/j.1365-246X.1958.tb00033.x

Lawson, C. L., & Hanson, R. J. (1995). *Solving least squares problems* (Vol. 15). Philadelphia, Pennsylvania, United States: Siam.

Lay, T., Ammon, C. J., Hutko, A. R., & Kanamori, H. (2010). Effects of kinematic constraints on teleseismic finite-source rupture inversions: Great Peruvian earthquakes of 23 June 2001 and 15 August 2007. *Bulletin of the Seismological Society of America*, *100*(3), 969–994.

Lay, T., & Kanamori, H. (1981). An asperity model of large earthquake sequences. In *Earthquake prediction*, *Maurice Ewing series*, (pp. 579–592). Washington, D. C: American Geophysical Union.

Lengliné, O., Enescu, B., Peng, Z., & Shiomi, K. (2012). Decay and expansion of the early aftershock activity following the 2011, M_w9. 0 Tohoku earthquake. *Geophysical Research Letters*, *39*, L18309. https://doi.org/10.1029/2012GL052797

Ligorría, J. P., & Ammon, C. J. (1999). Iterative deconvolution and receiver-function estimation. *Bulletin of the Seismological Society of America*, *89*(5), 1395–1400. https://doi.org/10.1016/S0304-3940(97)00816-1

Linde, A. T., Gladwin, M. T., Johnston, M. J. S., Gwyther, R. L., & Bilham, R. G. (1996). A slow earthquake sequence on the San Andreas fault. *Nature*, *383*(6595), 65.

Liu, Y., & Rice, J. R. (2005). Aseismic slip transients emerge spontaneously in three-dimensional rate and state modeling of subduction earthquake sequences. *Journal of Geophysical Research*, *110*, B08307. https://doi.org/10.1029/2004JB003424

Lohman, R. B., & McGuire, J. J. (2007). Earthquake swarms driven by aseismic creep in the Salton Trough, California. *Journal of Geophysical Research*, *112*, B04405. https://doi.org/10.1029/2006JB004596

Marone, C. J., Scholtz, C. H., & Bilham, R. (1991). On the mechanics of earthquake afterslip. *Journal of Geophysical Research*, *96*(B5), 8441–8452.

Matsu'ura, M., Kataoka, H., & Shibazaki, B. (1992). Slip-dependent friction law and nucleation processes in earthquake rupture. *Tectonophysics*, *211*(1–4), 135–148.

Matsu'ura, M., & Sato, T. (1989). A dislocation model for the earthquake cycle at convergent plate boundaries. *Geophysical Journal International*, *96*(1), 23–32.

Matsuzawa, T., Igarashi, T., & Hasegawa, A. (2002). Characteristic small-earthquake sequence off Sanriku, northeastern Honshu, Japan. *Geophysical Research Letters*, *29*(11), 1543. https://doi.org/10.1029/2001GL014632

McGuire, J. J., Boettcher, M. S., & Jordan, T. H. (2005). Foreshock sequences and short-term earthquake predictability on East Pacific Rise transform faults. *Nature*, *434*(7032), 457–461. https://doi.org/10.1038/nature03377

McGuire, J. J., & Jordan, T. H. (2000). Further evidence for the compound nature of slow earthquakes: The Prince Edward Island earthquake of April 28, 1997. *Journal of Geophysical Research*, *105*(B4), 7819–7827.

Mendoza, C., & Hartzell, S. H. (1988). Aftershock patterns and main shock faulting. *Bulletin of the Seismological Society of America*, *78*(4), 1438–1449.

Meneses-Gutierrez, A., & Sagiya, T. (2016). Persistent inelastic deformation in central Japan revealed by GPS observation before and after the Tohoku-oki earthquake. *Earth and Planetary Science Letters*, *450*, 366–371.

Miura, S., Iinuma, T., Yui, S., Uchida, N., Sato, T., Tachibana, K., & Hasegawa, A. (2006). Co- and post-seismic slip associated with the 2005 Miyagi-oki earthquake (M7.2) as inferred from GPS data. *Earth, Planets and Space*, *58*(12), 1567–1572.

Miyazaki, S., Segall, P., Fukuda, J., & Kato, T. (2004). Space time distribution of afterslip following the 2003 Tokachi-oki earthquake: Implications for variations in fault zone frictional properties. *Geophysical Research Letters*, *31*, L06623. https://doi.org/10.1029/2003GL019410

Mori, J., & Hartzell, S. (1990). Source inversion of the 1988 Upland, California, earthquake: determination of a fault plane for a small event. *Bulletin - Seismological Society of America*.

Moriya, H., Fujita, T., Niitsuma, H., Eisenblätter, J., & Manthei, G. (2006). Analysis of fracture propagation behavior using hydraulically induced acoustic emissions in the Bernburg salt mine, Germany. *International Journal of Rock Mechanics and Mining Sciences*, *43*(1), 49–57. https://doi.org/10.1016/j.ijrmms.2005.04.003

Murakami, M., Suito, H., Ozawa, S., & Kaidzu, M. (2006). Earthquake triggering by migrating slow slip initiated by M8 earthquake along Kuril Trench, Japan. *Geophysical Research Letters*, *33*, L09306. https://doi.org/10.1029/2006GL025967

Nadeau, R. M., & Johnson, L. R. (1998). Seismological studies at Parkfield VI: moment release rates and estimates of source parameters for small repeating earthquakes. *Bulletin of the Seismological Society of America*, *88*(3), 790–814.

Nakamura, W., Uchida, N., & Matsuzawa, T. (2016). Spatial distribution of the faulting types of small earthquakes around the 2011 Tohoku-oki earthquake: A comprehensive search using template events. *Journal of Geophysical Research: Solid Earth*, *121*, 2591–2607. https://doi.org/10.1002/2015JB012584

Nanjo, K. Z., Hirata, N., Obara, K., & Kasahara, K. (2012). Decade-scale decrease in b value prior to the *M*9-class 2011 Tohoku and 2004 Sumatra quakes. *Geophysical Research Letters*, *39*, L20304. https://doi.org/10.1029/2012GL052997

National Research Institute for Earth Science and Disaster Resilience (2019a). NIED Hi-net. Natl. Res. Inst. Earth Sci. Disaster Resil. https://doi.org/10.17598/NIED.0003

National Research Institute for Earth Science and Disaster Resilience (2019b). NIED K-NET, KiK-net. Natl. Res. Inst. Earth Sci. Disaster Resil. https://doi.org/10.17598/NIED.0004

Nishimura, T., Miura, S., Tachibana, K., Hashimoto, K., Sato, T., Hori, S., et al. (2000). Distribution of seismic coupling on the subducting plate boundary in northeastern Japan inferred from GPS observations. *Tectonophysics*, *323*(3–4), 217–238. https://doi.org/10.1016/S0040-1951(00)00108-6

Noda, A., Saito, T., & Fukuyama, E. (2018). Slip-deficit rate distribution along the Nankai Trough, Southwest Japan, with elastic lithosphere and viscoelastic asthenosphere. *Journal of Geophysical Research: Solid Earth*, *123*, 8125–8142. https://doi.org/10.1029/2018JB015515

Noda, A., Saito, T., Fukuyama, E., Terakawa, T., Tanaka, S., & Matsu'ura, M. (2020). 3-D spatial distribution of shear strain energy changes associated with the 2016 Kumamoto earthquake sequence, southwest Japan. *Geophysical Research Letters*, *47*, e2019GL086369. https://doi.org/10.1029/2019GL086369

Noda, H., Lapusta, N., & Kanamori, H. (2013). Comparison of average stress drop measures for ruptures with heterogeneous stress change and implications for earthquake physics. *Geophysical Journal International*, *193*(3), 1691–1712.

Ohnaka, M., & Kuwahara, Y. (1990). Characteristic features of local breakdown near a crack-tip in the transition zone from nucleation to unstable rupture during stick-slip shear failure. *Tectonophysics*, *175*(1–3), 197–220.

Okada, T., Matsuzawa, T., Umino, N., Yoshida, K., Hasegawa, A., Takahashi, H., et al. (2016). Hypocenter migration and crustal seismic velocity distribution observed for the inland earthquake swarms induced by the 2011 Tohoku-Oki earthquake in NE Japan: Implications for crustal fluid distribution and crustal permeability. *In Crustal Permeability*. https://doi.org/10.1002/9781119166573.ch24

Okada, Y. (1992). Internal deformation due to shear and tensile faults in a half-space. *Bulletin of the Geological Society of America*, *97*(B5), 7137–1040. https://doi.org/10.1029/92JB00178

Parotidis, M., Rothert, E., & Shapiro, S. A. (2003). Pore-pressure diffusion: A possible triggering mechanism for the earthquake swarms 2000 in Vogtland/NW-Bohemia, central Europe. *Geophysical Research Letters*, *30*(20), 2075. https://doi.org/10.1029/2003GL018110

Peng, Z., & Zhao, P. (2009). Migration of early aftershocks following the 2004 Parkfield earthquake. *Nature Geoscience*, *2*(12), 877.

Perfettini, H., & Avouac, J.-P. (2004). Postseismic relaxation driven by brittle creep: A possible mechanism to reconcile geodetic measurements and the decay rate of aftershocks, application to the Chi-Chi earthquake, Taiwan. *Journal of Geophysical Research*, *109*, B02304. https://doi.org/10.1029/2003JB002488

Perfettini, H., Frank, W. B., Marsan, D., & Bouchon, M. (2018). A model of aftershock migration driven by afterslip. *Geophysical Research Letters*, *45*, 2283–2293. https://doi.org/10.1002/2017GL076287

Pritchard, M. E., & Simons, M. (2006). An aseismic slip pulse in northern Chile and along-strike variations in seismogenic behavior. *Journal of Geophysical Research*, *111*, B08405. https://doi.org/10.1029/2006JB004258

Rice, J. R. (1992). Fault stress states, pore pressure distributions, and the weakness of the San Andreas fault. In *International geophysics* (Vol. 51, pp. 475–503). Massachusetts, Cambridge: Elsevier.

Rice, J. R., & Gu, J. (1983). Earthquake aftereffects and triggered seismic phenomena. *Pure and Applied Geophysics*, *121*(2), 187–219.

Roland, E., & McGuire, J. J. (2009). Earthquake swarms on transform faults. *Geophysical Journal International*, *178*(3), 1677–1690. https://doi.org/10.1111/j.1365-246X.2009.04214.x

Ross, Z. E., Hauksson, E., & Ben-Zion, Y. (2017). Abundant off-fault seismicity and orthogonal structures in the San Jacinto fault zone. *Science Advances*, *3*(3), e1601946. https://doi.org/10.1126/sciadv.1601946

Ross, Z. E., Idini, B., Jia, Z., Stephenson, O. L., Zhong, M., Wang, X., et al. (2019). Hierarchical interlocked orthogonal faulting in the 2019 Ridgecrest earthquake sequence. *Science*, *366*(6463), 346–351. https://doi.org/10.1126/science.aaz0109

Ross, Z. E., Kanamori, H., & Hauksson, E. (2017). Anomalously large complete stress drop during the 2016 M_w5.2 Borrego Springs earthquake inferred by waveform modeling and near-source aftershock deficit. *Geophysical Research Letters*, *44*, 5994–6001. https://doi.org/10.1002/2017GL073338

Ross, Z. E., Kanamori, H., Hauksson, E., & Aso, N. (2018). Dissipative intraplate faulting during the 2016 M_w6.2 Tottori, Japan earthquake. *Journal of Geophysical Research: Solid Earth*, *123*, 1631–1642. https://doi.org/10.1002/2017JB015077

Ryder, I., & Bürgmann, R. (2008). Spatial variations in slip deficit on the central San Andreas fault from InSAR. *Geophysical Journal International*, *175*(3), 837–852.

Saito, T., & Noda, A. (2020). Strain energy released by earthquake faulting with random slip components. *Geophysical Journal International*, *220*(3), 2009–2020.

Saito, T., Noda, A., Yoshida, K., & Tanaka, S. (2018). Shear strain energy change caused by the interplate coupling along the Nankai Trough: An integration analysis using stress tensor inversion and slip-deficit inversion. *Journal of Geophysical Research: Solid Earth*, *123*, 5975–5986. https://doi.org/10.1029/2018JB015839

Savage, J. C. (1969). Steketee's paradox. *Bulletin of the Seismological Society of America*, *59*(1), 381–384.

Savage, J. C. (1983). A dislocation model of strain accumulation and release at a subduction zone. *Journal of Geophysical Research*, *88*(B6), 4984–4996.

Schaff, D. P., Beroza, G. C., & Shaw, B. E. (1998). Postseismic response of repeating aftershocks. *Geophysical Research Letters*, *25*(24), 4549–4552.

Shao, G., Ji, C., & Hauksson, E. (2012). Rupture process and energy budget of the 29 July 2008 M_w5.4 Chino Hills, California, earthquake. *Journal of Geophysical Research*, *117*, B07307. https://doi.org/10.1029/2011JB008856

Shapiro, S. A., Huenges, E., & Borm, G. (1997). Estimating the crust permeability from fluid-injection-induced seismic emission at the KTB site. *Geophysical Journal International*, *131*(2). https://doi.org/10.1111/j.1365-246X.1997.tb01215.x

Shelly, D. R., Hill, D. P., Massin, F., Farrell, J., Smith, R. B., & Taira, T. (2013). A fluid-driven earthquake swarm on the margin of the Yellowstone caldera. *Journal of Geophysical Research: Planets*, *118*, 4872–4886. https://doi.org/10.1002/jgrb.50362

Shelly, D. R., Moran, S. C., & Thelen, W. A. (2013). Evidence for fluid-triggered slip in the 2009 Mount Rainier, Washington earthquake swarm. *Geophysical Research Letters*, *40*, 1506–1512. https://doi.org/10.1002/grl.50354

Shelly, D. R., Taira, T., Prejean, S. G., Hill, D. P., & Dreger, D. S. (2015). Fluid-faulting interactions: Fracture-mesh and fault-valve behavior in the February 2014 Mammoth Mountain, California, earthquake swarm. *Geophysical Research Letters*, *42*, 5803–5812. https://doi.org/10.1002/2015GL064325

Shi, Y., & Bolt, B. A. (1982). The standard error of the magnitude-frequency *b* value. *Bulletin of the Seismological Society of America*, *72*(5), 1677–1687.

Shibazaki, B., & Iio, Y. (2003). On the physical mechanism of silent slip events along the deeper part of the seismogenic zone. *Geophysical Research Letters*, *30*(9), 1489. https://doi.org/10.1029/2003GL017047

Shimamura, K., Matsuzawa, T., Okada, T., Uchida, N., Kono, T., & Hasegawa, A. (2011). Similarities and differences in the rupture process of the $M \sim 4.8$ repeating-earthquake sequence off Kamaishi, Northeast Japan: Comparison between the 2001 and 2008 events. *Bulletin of the Seismological Society of America*, *101*(5), 2355–2368.

Sibson, R. H. (1992). Implications of fault-valve behaviour for rupture nucleation and recurrence. *Tectonophysics*, *211*(1–4), 283–293. https://doi.org/10.1016/0040-1951(92)90065-E

Smith, D. E., & Dieterich, J. H. (2010). Aftershock sequences modeled with 3-D stress heterogeneity and rate-state seismicity equations: Implications for crustal stress estimation. In *Seismogenesis and earthquake forecasting: The Frank Evison volume II* (pp. 213–231). New York City: Springer.

Smith, D. E., & Heaton, T. H. (2011). Models of stochastic, spatially varying stress in the crust compatible with focal-mechanism data, and how stress inversions can be biased toward the stress rate. *Bulletin of the Seismological Society of America*, *101*(3), 1396–1421. https://doi.org/10.1785/0120100058

Suwa, Y., Miura, S., Hasegawa, A., Sato, T., & Tachibana, K. (2006). Interplate coupling beneath NE Japan inferred from three-dimensional displacement field. *Journal of Geophysical Research*, *111*, B04402. https://doi.org/10.1029/2004JB003203

Suyehiro, S. (1966). Difference between aftershocks and foreshocks in the relationship of magnitude to frequency of occurrence for the great Chilean earthquake of 1960. *Bulletin of the Seismological Society of America*, *56*(1), 185–200.

Tamaribuchi, K., Yagi, Y., Enescu, B., & Hirano, S. (2018). Characteristics of foreshock activity inferred from the JMA earthquake catalog. *Earth, Planets and Space*, *70*(1), 90.

Terakawa, T., Hashimoto, C., & Matsu'ura, M. (2013). Changes in seismic activity following the 2011 Tohoku-oki earthquake: Effects of pore fluid pressure. *Earth and Planetary Science Letters*, *365*, 17–24. https://doi.org/10.1016/j.epsl.2013.01.017

Tormann, T., Wiemer, S., Enescu, B., & Woessner, J. (2016). Normalized rupture potential for small and large earthquakes along the Pacific Plate off Japan. *Geophysical Research Letters*, *43*, 7468–7477. https://doi.org/10.1002/2016GL069309

Tse, S. T., & Rice, J. R. (1986). Crustal earthquake instability in relation to the depth variation of frictional slip properties. *Journal of Geophysical Research*, *91*(B9), 9452–9472.

Uchida, N., Hasegawa, A., Matsuzawa, T., & Igarashi, T. (2004). Pre- and post-seismic slow slip on the plate boundary off Sanriku, NE Japan associated with three interplate earthquakes as estimated from small repeating earthquake data. *Tectonophysics*, *385*(1–4), 1–15.

Uchida, N., & Matsuzawa, T. (2013). Pre- and postseismic slow slip surrounding the 2011 Tohoku-oki earthquake rupture. *Earth and Planetary Science Letters*, *374*, 81–91.

Uchida, N., Yui, S., Miura, S., Matsuzawa, T., Hasegawa, A., Motoya, Y., & Kasahara, M. (2009). Quasi-static slip on the plate boundary associated with the 2003 M8.0 Tokachi-oki and 2004 M7.1 off-Kushiro earthquakes, Japan. *Gondwana Research*, *16*(3–4), 527–533.

Urata, Y., Yoshida, K., Fukuyama, E., & Kubo, H. (2017). 3-D dynamic rupture simulations of the 2016 Kumamoto, Japan, earthquake. 4. Seismology. *Earth, Planets and Space*, *69*(1), 150. https://doi.org/10.1186/s40623-017-0733-0

Vassiliou, M. S., & Kanamori, H. (1982). The energy release in earthquakes. *Bulletin of the Seismological Society of America*, *72*(2), 371–387.

Venkataraman, A., & Kanamori, H. (2004). Observational constraints on the fracture energy of subduction zone earthquakes. *Journal of Geophysical Research*, *109*, B05302. https://doi.org/10.1029/2003JB002549

Vidale, J. E., Boyle, K. L., & Shearer, P. M. (2006). Crustal earthquake bursts in California and Japan: Their patterns and relation to volcanoes. *Geophysical Research Letters*, *33*(20), 1–5. https://doi.org/10.1029/2006GL027723

Vidale, J. E., & Shearer, P. M. (2006). A survey of 71 earthquake bursts across southern California: Exploring the role of pore fluid pressure fluctuations and aseismic slip as drivers. *Journal of Geophysical Research*, *111*, B05312. https://doi.org/10.1029/2005JB004034

Viesca, R. C., & Dublanchet, P. (2019). The slow slip of viscous faults. *Journal of Geophysical Research: Solid Earth*, *124*(5), 4959–4983.

Waldhauser, F., & Ellsworth, W. L. (2000). A double-difference earthquake location algorithm: Method and application to the northern Hayward Fault, California. *Bulletin of the Seismological Society of America*, *90*(6), 1353–1368. https://doi.org/10.1785/0120000006

Wang, L., Hainzl, S., Zöller, G., & Holschneider, M. (2012). Stress- and aftershock-constrained joint inversions for coseismic and post-seismic slip applied to the 2004 M6.0 Parkfield earthquake. *Journal of Geophysical Research*, *117*, B07406. https://doi.org/10.1029/2011JB009017

Wessel, P., & Smith, W. H. F. (1998). New, improved version of generic mapping tools released. *Eos, Transactions American Geophysical Union*, *79*(47), 579–579. https://doi.org/10.1029/98EO00426

Wesson, R. L. (1987). Modelling aftershock migration and afterslip of the San Juan Bautista, California, earthquake of October 3, 1972. *Tectonophysics*, *144*(1–3), 215–229.

Wetzler, N., Lay, T., Brodsky, E. E., & Kanamori, H. (2018). Systematic deficiency of aftershocks in areas of high coseismic slip for large subduction zone earthquakes. *Science Advances*, *4*(2), 1–10. https://doi.org/10.1126/sciadv.aao3225

Woessner, J., Schorlemmer, D., Wiemer, S., & Mai, P. M. (2006). Spatial correlation of aftershock locations and on-fault main shock properties. *Journal of Geophysical Research*, *111*, B08301. https://doi.org/10.1029/2005JB003961

Xia, K., Rosakis, A. J., & Kanamori, H. (2004). Laboratory earthquakes: The sub-Rayleigh-to-supershear rupture transition. *Science*, *303*(5665), 1859–1861.

Xue, L., Bürgmann, R., Shelly, D. R., Johnson, C. W., & Taira, T. (2018). Kinematics of the 2015 San Ramon, California earthquake swarm: Implications for fault zone structure and driving mechanisms. *Earth and Planetary Science Letters*, *489*, 135–144. https://doi.org/10.1016/j.epsl.2018.02.018

Yabe, S., & Ide, S. (2018). Variations in precursory slip behavior resulting from frictional heterogeneity. *Progress in Earth and Planetary Science*, *5*(1), 43.

Yabe, Y., Nakatani, M., Naoi, M., Philipp, J., Janssen, C., Watanabe, T., et al. (2015). Nucleation process of an M2 earthquake in a deep gold mine in South Africa inferred from on-fault foreshock activity. *Journal of Geophysical Research: Solid Earth*, *120*, 5574–5594. https://doi.org/10.1002/2014JB011680

Yamanaka, Y., & Kikuchi, M. (2004). Asperity map along the subduction zone in northeastern Japan inferred from regional seismic data. *Journal of Geophysical Research*, *109*, B07307. https://doi.org/10.1029/2003JB002683

Yoshida, K. (2019). Prevalence of asymmetrical rupture in small earthquakes and its effect on the estimation of stress drop: A systematic investigation in inland Japan. *Geoscience Letters*, *6*(1), 16.

Yoshida, K., & Hasegawa, A. (2018a). Hypocenter migration and seismicity pattern change in the Yamagata-Fukushima border, NE Japan, caused by fluid movement and pore pressure variation. *Journal of Geophysical Research: Solid Earth*, *123*, 5000–5017. https://doi.org/10.1029/2018JB015468

Yoshida, K., & Hasegawa, A. (2018b). Sendai-Okura earthquake swarm induced by the 2011 Tohoku-Oki earthquake in the stress shadow of NE Japan: Detailed fault structure and hypocenter migration. *Tectonophysics*, *733*(August 2017), 132–147. https://doi.org/10.1016/j.tecto.2017.12.031

Yoshida, K., Hasegawa, A., & Okada, T. (2015). Spatially heterogeneous stress field in the source area of the 2011 M_w 6.6 Fukushima-Hamadori earthquake, NE Japan, probably caused by static stress change. *Geophysical Journal International*, *201*(2), 1062–1071. https://doi.org/10.1093/gji/ggv068

Yoshida, K., Hasegawa, A., & Okada, T. (2016). Heterogeneous stress field in the source area of the 2003 M6.4 Northern Miyagi Prefecture, NE Japan, earthquake. *Geophysical Journal International*, *206*(1), 408–419. https://doi.org/10.1093/gji/ggw160

Yoshida, K., Hasegawa, A., Okada, T., & Iinuma, T. (2014). Changes in the stress field after the 2008 *M*7.2 Iwate-Miyagi Nairiku earthquake in northeastern Japan. *Journal of Geophysical Research: Solid Earth*, *119*, 9016–9030. https://doi.org/10.1002/2014JB011291

Yoshida, K., Hasegawa, A., Okada, T., Iinuma, T., Ito, Y., & Asano, Y. (2012). Stress before and after the 2011 great Tohoku-oki earthquake and induced earthquakes in inland areas of eastern Japan. *Geophysical Research Letters*, *39*, L03302. https://doi.org/10.1029/2011GL049729

Yoshida, K., Hasegawa, A., & Yoshida, T. (2016a). Temporal variation of frictional strength in an earthquake swarm in NE Japan caused by fluid migration. *Journal of Geophysical Research: Solid Earth*, *121*, 5953–5965. https://doi.org/10.1002/2016JB013022

Yoshida, K., Hasegawa, A., & Yoshida, T. (2016b). Temporal variation of frictional strength in an earthquake swarm in NE Japan caused by fluid migration. *Journal of Geophysical Research: Solid Earth*, *121*(8), 5953–5965. https://doi.org/10.1002/2016JB013022

Yoshida, K., Hasegawa, A., Yoshida, T., & Matsuzawa, T. (2019). Heterogeneities in stress and strength in Tohoku and its relationship with earthquake sequences triggered by the 2011 M9 Tohoku-Oki earthquake. *Pure and Applied Geophysics*, *176*(3), 1335–1355.

Yoshida, K., Saito, T., Emoto, K., Urata, Y., & Sato, D. (2019). Rupture directivity, stress drop, and hypocenter migration of small- and moderate-sized earthquakes in the Yamagata-Fukushima border swarm triggered by upward pore-pressure migration after the 2011 Tohoku-Oki earthquake. *Tectonophysics*.

Yoshida, K., Saito, T., Urata, Y., Asano, Y., & Hasegawa, A. (2017). Temporal changes in stress drop, frictional strength, and earthquake size distribution in the 2011 Yamagata-Fukushima, NE Japan, earthquake swarm, caused by fluid migration. *Journal of Geophysical Research: Solid Earth*, *122*, 10,379–10,397. https://doi.org/10.1002/2017JB014334

Yukutake, Y., Ito, H., Honda, R., Harada, M., Tanada, T., & Yoshida, A. (2011). Fluid-induced swarm earthquake sequence revealed by precisely determined hypocenters and focal mechanisms in the 2009 activity at Hakone volcano, Japan. *Journal of Geophysical Research*, *116*, B04308. https://doi.org/10.1029/2010JB008036